

# Addendum: SPT-Based Probabilistic Liquefaction Models

#### March 2024

K. J. Ulmer<sup>1</sup>

K. S. Hudson<sup>2,3</sup>

S. J. Brandenberg<sup>2</sup>

P. Zimmaro<sup>4,2</sup>

S. L. Kramer<sup>5</sup>

J. P. Stewart<sup>2</sup>

<sup>1</sup>Southwest Research Institute San Antonio, Texas

<sup>2</sup>University of California, Los Angeles Los Angeles, California

<sup>3</sup>Hudson Geotechnics, Inc. El Segundo, California

<sup>4</sup>University of Calabria Arcavacata di Rende, Italy

<sup>5</sup>University of Washington Seattle, Washington

Thomas Weaver, NRC Project Manager

Research Information Letter Office of Nuclear Regulatory Research

# **Disclaimer**

Legally binding regulatory requirements are stated only in laws, NRC regulations, licenses, including technical specifications, or orders; not in Research Information Letters (RILs). A RIL is not regulatory guidance, although NRC's regulatory offices may consider the information in a RIL to determine whether any regulatory actions are warranted.

#### **PREFACE**

This is an addendum to a companion report, referred to herein as the Task 7 report (Ulmer et al., 2024), which presented probabilistic models for liquefaction susceptibility, triggering, and manifestation that use inputs from a cone penetrometer test (CPT). The objective of this addendum is to document the development of probabilistic models that take as input soil stratigraphy from borehole logs, available laboratory index test results, and penetration resistance measurements from standard penetration tests (SPT). For brevity, this type of site characterization is referred to subsequently as "SPT-based site characterization." This addendum fulfills Task 9 of the current contract jointly supported by the U.S. Nuclear Regulatory Commission (NRC) and the U.S. Bureau of Reclamation (USBR).

In the Task 7 report, the Supported Modeling Team (SMT) presented probabilistic models based on CPT data. Many of the foundational elements of those CPT-based models are common to the SPT-based models outlined in this addendum. Thus, only the unique SPT-related elements are discussed in this addendum, with appropriate references to the Task 7 report. Moreover, we apply notation and variable names in this report that were defined in the Task 7 report without re-defining them here. Accordingly, readers interested in looking up definitions of terms (such as P[T|S]) are encouraged to consult the Task 7 report.

In Chapter 10, we describe the steps required to develop the necessary stratigraphic parameters and soil properties from SPT-based site characterizations for use in model development. In Chapter 11, we provide SPT-based models, including (i) an equation to compute the probability of susceptibility to liquefaction in a given soil layer and (ii) an equation to compute the probability of triggering. We also outline a framework to develop equations to compute the probability of surface manifestation and check the reasonableness of using the CPT-based manifestation model based on depth to the top of the soil layer. In Chapter 12 we outline the limitations of the models presented in this addendum, discuss important aspects of using these SPT-based models, and identify future work that has the potential to improve model performance. Finally, we summarize the conclusions of our work in Chapter 13.

Our findings provided in the Task 7 report and this addendum are nearing their final form, although future refinements and improvements are possible. The content presented here is subject to change as we refine the methodologies, input parameters, and framework. Although the SPT- and CPT-based models rely on several common elements, the SPT-based manifestation models are less mature than the CPT-based models, due in part to challenges with interpreting SPT-based case histories and inconsistent data density, as discussed in Section 12.1, and due to limitations of the project schedule. Opportunities for future work listed in Section 12.3 may address the discrepancy in model refinement and maturity.

While the general concepts behind our approach and the CPT-based models have been shared in meetings with the Next Generation Liquefaction (NGL) Advisory Board, the MRT, and other NGL modeling teams, this addendum presents new relationships specifically for applications using SPT-based site characterization data. Accordingly, we welcome feedback on these specific relationships from the liquefaction research community as they mature and feedback from regulatory agencies, topical experts, practicing engineers, and others about the modeling approach and the reasonableness and practicality for application of the models that have been presented.

## Reference

Ulmer, K.J., K.S. Hudson, S.J. Brandenberg, P. Zimmaro, R. Pretell, B. Carlton, S.L. Kramer, and J.P. Stewart. "Task 7C: Next Generation Liquefaction Models for Susceptibility, Triggering, and Manifestation." Washington, DC: U.S. Nuclear Regulatory Commission. March 2024.

# **TABLE OF CONTENTS**

		Page
TABI LIST LIST LIST ABB	FACE LE OF CONTENTS OF FIGURES OF TABLES OF SYMBOLS REVIATION/ACRONYMS	vii vii xi xi
ACK	NOWLEDGMENT	XV
10	SPT CASE HISTORY PROCESSING	10-1
	10.1 Assigning Observations to In Situ Tests	
	10.2 Layer Boundaries	
	10.3 Assigning Layer Properties	
	10.3.1 Estimation of PI and FC	
	10.3.1.1 Representative PI and FC based on measurements.	10-6
	10.3.1.2 Representative PI and FC without measurements	10-8
	10.3.2 Penetration Resistance and Stress Normalization	10-14
	10.3.3 Cyclic Stress Ratio	10-17
11	SPT-BASED MODELS	11-1
	11.1 Probability of Susceptibility, P[S]	11-1
	11.1.1 P[S] as a Function of PI	11-1
	11.1.2 P[S] as a Function of Soil Description Alone	11-3
	11.2 Probability of Triggering, P[T S]	11-6
	11.3 Example Comparisons of SPT and CPT Triggering Models	11-11
	11.4 Probability of Manifestation P[M] Model Framework	
	11.4.1 Manifestation Probability for a Profile	
	11.4.2 Profile-Based Regression Framework	
	11.5 Consistency of SPT Data with CPT P[M] Model	11-19
12	DISCUSSION OF BOREHOLE AND SPT-BASED MODELS	
	12.1 Challenges in Interpreting Borehole Data	
	12.2 Triggering and Manifestation	
	12.3 Future Work	12-5
13	CONCLUSIONS, SPT-BASED MODELS	13-1
14	REFERENCES	14-1
	ENDIX A—PARAMETERS IN THE SUMMARY pki FILE CONTAINING SMT'S CESSED CASE HISTORY DATA	

# **LIST OF FIGURES**

		Page
Figure 10-1	A screenshot of the Jupyter notebook that the SMT designed for reviews of individual case histories. Black markers represent observations of "no manifestation", red markers represent "yes manifestation", green markers represent boreholes, red/black lines connect boreholes and observations that the SMT grouped together, and red/black circles indicate a co-located borehole and observation pair. Case history: Mihama Ward, 2011 Tohoku earthquake.	10-3
Figure 10-2	A screenshot of the Jupyter notebook that the SMT designed for reviews of layer boundaries and assigned layer properties for individual case histories.	10-5
Figure 10-3	Histogram of the variance of <i>PI</i> within layers. The mean is represented by the dashed vertical black line. The dataset used to compute these variances includes <i>PI</i> measurements from 65 layers that have more than one Atterberg limit test performed within the STRA table defined layer.	10-7
Figure 10-4	Histogram of the variance of <i>FC</i> within layers. The mean is represented by the dashed vertical black line. The dataset used to compute these variances includes <i>FC</i> measurements from 287 layers that have more than one grain size distribution test performed within the STRA table defined layer.	10-7
Figure 10-5	Distributions of <i>PI</i> within each soil type group. The blue shaded area represents an approximate histogram of the data, with box and whisker plots in black. Medians are represented by an orange bar, and means are reported at the top of each plot.	10-9
Figure 10-6	Distributions of <i>FC</i> within each soil type group. The blue shaded area represents an approximate histogram of the data, with box and whisker plots in black. Medians are represented by an orange bar, and means are reported at the top of each plot.	10-9
Figure 10-7	Box-Cox transformations for PI in each soil type group.	10-11
Figure 10-8	Box-Cox transformations for FC in each soil type group	.10-13
Figure 10-9	Histogram of the variance of N within layers. The mean is represented by the dashed vertical black line. The dataset used to compute these variances includes <i>N</i> from 227 layers that have more than one SPT performed within a single STRA-defined layer.	.10-15

Figure 11-1	Digitized datapoints from (a) Bray and Sancio (2006) and (b) Boulanger and Idriss (2006) with susceptibility labels S = susceptible, MS = marginally susceptible, and NS = not susceptible. Thin lines represent probability density functions for each susceptibility label and the thick black lines represent the SMT's P[S] models as a function of PI using Eq. (11-1).
Figure 11-2	P[S] models based on Bray and Sancio (2006), Boulanger and Idriss (2006), and the SMT's combined model. The dashed line represents an average between the BS06 and BI06 models
Figure 11-3	Comparison of the SMT's <i>PI</i> -based P[ <i>S</i> ] model with the SMT's P[ <i>S</i> ] estimates based on text descriptions. Shaded areas represent relative distributions of <i>PI</i> in each soil type group, centered vertically on the assigned P[ <i>S</i> ] for that soil type group.
Figure 11-4	Comparison of the SMT's $I_c$ -based P[S] model (blue line and circles) with the P[S] models based on Bray and Sancio (2006), Boulanger and Idriss (2006), and the SMT's combined model. Estimates of $I_c$ for each soil type group are approximated based on descriptions from Robertson and Cabal (2015)
Figure 11-5	Comparison of the Idriss and Boulanger (2008) correlation between $D_r$ and a) $N_{1,60}$ and b) $N_{1,60cs}$ for three fitting coefficients: $C_d$ = 35, 46, and 60. The SMT adopted the relationship with $C_d$ = 46
Figure 11-6	Plots of $D_r$ -dependence of (a) $CRR$ and (b) $PF_{T S}$
Figure 11-7	Plots of $N_{1,60cs}$ -dependence of (a) $CRR$ and (b) $PF_{T S}$ . Dotted lines indicate where $N_{1,60cs}$ would yield a $D_r > 100\%$ using the adopted correlation
Figure 11-8	Map of Moss Landing Harbor Office area (Boulanger et al., 1995, 1997)11-12
Figure 11-9	A screenshot of the SMT's Jupyter tool showing layer boundaries and representative layer characteristics for UC-B3 at Moss Landing Harbor Office
Figure 11-10	Comparison of the SMT's SPT- and CPT-based models using CPT data (UC-21) and SPT data (UC-B3) at Moss Landing Harbor Office. (a) $q_{c1Ncs}$ , (b) $I_c$ , (c) $N_{160cs}$ , (d) $CSR_{M7.5,1atm}$ , I $CRR$ , (f) $P[T S]$ , and (g) $P[S]$ 11-14
Figure 11-11	Comparison of the BI12 SPT-based models and the BI16 CPT-based models using CPT data (UC-21) and SPT data (UC-B3) at Moss Landing Harbor Office. (a) $q_{c1Ncs}$ , (b) $I_c$ , (c) $N_{160cs}$ , (d) $CSR_{M7.5,1atm}$ , I $CRR$ , (f) $P[T S]$ , and (g) $P[S]$
Figure 11-12	Comparison of the BI12 SPT-based models and the SMT's SPT-based models using SPT data (UC-B3) at Moss Landing Harbor Office. (a) $q_{c1Ncs}$ , (b) $I_c$ , (c) $N_{160cs}$ , (d) $CSR_{M7.5.1atm}$ , (e) $CRR$ , (f) $P[T S]$ , and (g) $P[S]$ 11-16

Figure 11-13	Performance of the CPT-based $PF_{M T}(z_{top})$ model used with the SPT dataset of reviewed profiles with a measured $N$ value within each layer. (a), (b), and (c) present the model parameters in the relevant dataspaces for $PF_{M T}$ , $PF_{T S}$ , and $PF_{S}$ , respectively. (d) presents the confusion matrix and statistical metrics of the predicted $P[M_P]$ using the model parameters in (a), (b), and (c) compared with the observation of manifestation for each of the SPT case histories in the reduced dataset	11-20
Figure 11-14	Performance of the $PF_{M T}(z_{top})$ model regressed using CPT data on the CPT dataset (Task 7 report).	11-21
Figure 11-15	Performance of the CPT-based $PF_{M T}(z_{top})$ model used with the SPT dataset of all reviewed profiles. (a), (b), and (c) present the model parameters in the relevant dataspaces for $PF_{M T}$ , $PF_{T S}$ , and $PF_{S}$ , respectively. (d) presents the confusion matrix and statistical metrics of the predicted $P[M_P]$ using the model parameters in (a), (b), and (c) compared with the observation of manifestation for each of the SPT case histories in the full dataset.	11-22
Figure 11-16	Performance of the $P[M_P]$ model where $PF_{M T}$ is set to 1 for all layers in the SPT dataset of all reviewed profiles. (a), (b), and (c) present the model parameters in the relevant dataspaces for $PF_{M T}$ , $PF_{T S}$ , and $PF_{S}$ , respectively. (d) presents the confusion matrix and statistical metrics of the predicted $P[M_P]$ using the model parameters in (a), (b), and (c) compared with the observation of manifestation for each of the SPT case histories in the full dataset.	11-24
Figure 11-17	Performance of the $P[M_P]$ model where $PF_{M T}$ is set to 1 for all layers in the SPT dataset of all reviewed profiles and $PF_{T S}$ is set to the Boulanger and Idriss (2012) model. (a), (b), and (c) present the model parameters in the relevant dataspaces for $PF_{M T}$ , $PF_{T S}$ , and $PF_S$ , respectively. (d) presents the confusion matrix and statistical metrics of the predicted $P[M_P]$ using the model parameters in (a), (b), and (c) compared with the observation of manifestation for each of the SPT case histories in the full dataset.	11-25

# **LIST OF TABLES**

		Page
Table 10-1	Soil type groups for <i>PI</i> and <i>FC</i> distributions	10-10
Table 10-2	$\lambda_{Pl}$ , mean $PI$ , standard deviation of $PI$ , and mean $Pl$ from Box-Cox transformation for each soil type group	10-12
Table 10-3	$\lambda_{FC}$ , Mean $FC$ , and standard deviation of $FC$ from Box-Cox transformation and mean $FC$ for each soil type group	10-14
Table 11-1	Coefficients in Eq. (11-1) for three P[S] models	11-3
Table 11-2	Mean <i>PI</i> , standard deviation of <i>PI</i> , and associated P[ <i>S</i> ] from the combined SMT model for each soil type group	11-4

#### LIST OF SYMBOLS

#### **Symbols**

CSR<sub>M7.5,1atm</sub> CSR corrected for M7.5 and 1 atm of overburden stress

CRR cyclic resistance ratio

*D<sub>r</sub>* relative density

FC percent fines content by weight, fines are defined as particles smaller than

0.075 mm

*l<sub>c</sub>* soil behavior type index

K<sub>sat</sub> saturation correction factor

 $K_{\sigma}$  initial overburden stress adjustment factor

LL liquid limit from Atterberg limits tests

**M** earthquake magnitude, typically moment magnitude

MSF magnitude scaling factor

N SPT blow count

 $N_1$  N adjusted for overburden stress  $N_{1,60}$   $N_1$  adjusted for 60% applied energy  $N_{1,60cs}$   $N_{1,60}$  adjusted for clean sand conditions

PGA peak ground acceleration, generally taken as median component

PI plasticity index, or LL – PL

PL plastic limit from Atterberg limits tests

 $q_c$  cone tip resistance from CPT

 $q_{c1N}$   $q_c$  adjusted for 1 atm overburden (through  $C_N$ )

 $q_{c1Ncs}$   $q_{c1N}$  adjusted for clean sand conditions

r<sub>d</sub> shear stress reduction factor

 $\sigma_{v}$  total vertical stress

 $\sigma'_{v0}$  initial vertical effective stress

t<sub>c</sub> characteristic layer thickness

 $w_c$  water content

z depth measured from ground surface

P[T] probability of triggering

P[7|S] probability of triggering conditioned on the soil being susceptible

P[M|T] probability of manifestation given triggering

P[M|NT]  $P[M_L]$   $P[M_P]$  P[S]probability of manifestation given no triggering probability of manifestation of a layer probability of manifestation of the profile probability of susceptibility

#### **ACRONYMS/ABBREVIATIONS**

Bl06 Boulanger and Idriss (2006) susceptibility criterion

BI12 Boulanger and Idriss (2012)
BI14 Boulanger and Idriss (2014)
BI16 Boulanger and Idriss (2016)

BS06 Bray and Sancio (2006) susceptibility criterion

CPT cone penetrometer test

FLDM field manifestation (e.g., FLDM ID in the NGL database)

GMIM ground motion intensity measure

GUI graphical user interface

MRT Model Review Team

NGL Next Generation Liquefaction

NRC U.S. Nuclear Regulatory Commission

NUTS No-U-Turn Hamiltonian Monte Carlo sampling

PGA peak ground attenuation

SAMP samples

SFEV surface evidence tag (0 = no surface manifestation, 1 = yes surface

manifestation)

SMT Supported Modeling Team SPT standard penetration test SQL structured query language

STRA stratigraphy

U.S. United States

#### **ACKNOWLEDGMENTS**

This report was prepared to document work performed by the Geoscience and Engineering Department (GED) at Southwest Research Institute® and its partners for the U.S. Nuclear Regulatory Commission (NRC) under Contract No. 31310018D0002 and through an interagency agreement with the U.S. Bureau of Reclamation (Agreement Number R20PG00126). The activities reported here were performed on behalf of the NRC Office of Nuclear Regulatory Research. The report is an independent product of GED and does not necessarily reflect the views or regulatory position of the NRC.

The authors wish to acknowledge members of the Next Generation Liquefaction (NGL) community for their contributions to the aims of NGL that have supported this work.

We also gratefully acknowledge Lane Howard for project management, John Stamatakos for technical review of this report, and Arturo Ramos for administrative support.

## QUALITY OF DATA, ANALYSES, AND CODE DEVELOPMENT

**DATA**: The primary data source for the work described herein is the NGL database (<a href="http://nextgenerationliquefaction.org">http://nextgenerationliquefaction.org</a>, doi: 10.21222/C23P70, Ulmer et al., 2023; Brandenberg et al., 2020). The NGL database contains data related to case histories of earthquake-induced liquefaction. These data are from the geotechnical community, including academic researchers and practicing engineers. Because the intent of the database is to accumulate as much useful and publicly available data as possible from the technical community, some of the data are from existing scientific and technical publications and peer-reviewed journals, but some could also be sourced from the working records of researchers and engineers. The data are uploaded to the database via a graphical user interface (GUI). Reviewers evaluate the quality of data after it is uploaded to provide quality control (Zimmaro et al., 2019). Data that has not yet been reviewed is marked as such in the database. For other data references in the database, such as the earthquake records from the Next Generation Attenuation project series, users should consult the original sources to determine the level of quality of those data.

Other data sources are cited throughout the report and stored in project folders PRJ-3368 and PRJ-2923 on DesignSafe-CI (Rathje et al., 2017).

**ANALYSES AND CODES**: The NGL database is a relational database that was developed using the My Structured Query Language (MySQL) relational database management system. The NGL database schema (i.e., its organizational structure) and a meta-dictionary that contains information about each database entry are available at http://nextgenerationliquefaction.org (Brandenberg et al., 2020).

#### **REFERENCES**

Brandenberg, S.J., P. Zimmaro, J.P. Stewart, D.Y. Kwak, K.W. Franke, R.E.S. Moss, K.O. Çetin, G. Can, M. Ilgac, J. Stamatakos, T. Weaver, and S.L. Kramer. "Next-Generation Liquefaction Database." *Earthquake Spectra*. Vol. 36, No. 2. pp. 939–959. 2020.

Rathje, E., C. Dawson, J.E. Padgett, J.-P. Pinelli, D. Stanzione, A. Adair, P. Arduino, S.J. Brandenberg, T. Cockerill, C. Dey, M. Esteva, F.L. Haan, Jr., M. Hanlon, A. Kareem, L. Lowes, S. Mock, and G. Mosqueda. "DesignSafe: A New Cyberinfrastructure for Natural Hazards Engineering." *ASCE Natural Hazards Review.* Vol. 18, No. 3. doi:10.1061/(ASCE)NH.1527-6996.0000246. 2017.

Ulmer, K.J., P. Zimmaro, S.J. Brandenberg, J.P. Stewart, K.S. Hudson, A.W. Stuedlein, A. Jana, A. Dadashiserej, S.L. Kramer, K.O. Cetin, G. Can, M. Ilgac, K.W. Franke, R.E.S. Moss, S.F. Bartlett, M. Hosseinali, H. Dacayanan, DY. Kwak, J. Stamatakos, J. Mukherjee, U. Salman, S. Ybarra, and T. Weaver. "Next-Generation Liquefaction Database." Version 2. Next-Generation Liquefaction Consortium. doi: 10.21222/C23P70. 2023.

Zimmaro, P., S.J. Brandenberg, Y. Bozorgnia, J.P. Stewart, D.Y. Kwak, K.O. Cetin, G. Can, M. Ilgac, K.W. Franke, R.E.S. Moss, S.L. Kramer, J. Stamatakos, M. Juckett, and T. Weaver. "Quality Control for Next-generation Liquefaction Case Histories." Proceeding of the 7<sup>th</sup> International Conference on Earthquake Geotechnical Engineering (VII ICEGE). Rome (Italy). June 17-20, 2019. pp. 5,905–5,912. 2019.

#### 10 SPT CASE HISTORY PROCESSING

Case history processing is required to convert data (e.g., stratigraphy from borehole logs, SPT *N* values, groundwater table measurements, ground motion measurements, observations of liquefaction manifestation) into metrics that facilitate development of liquefaction triggering models (e.g., *CSR*, *N*<sub>1,60cs</sub>). The goal of processing SPT-based site characterization data is to couple liquefaction observations (or lack thereof) to a set of nearby boreholes and to identify and characterize layers within each borehole. This is needed to perform liquefaction evaluation calculations at depth. Our approach to processing SPT-based site characterization data initially uses automated procedures to assign observations to boreholes, determine layer boundaries, and estimate soil properties to characterize the layers. We augment these automated processes with judgment through human reviews of individual case histories. Whenever feasible, we codify our judgments so that they are objective and reproducible by other analysts. The development of calibrated automated processes is crucial for analyzing a database as large as the NGL database, and provides a repeatable, consistent, and objective initial view of the data.

This chapter describes the steps required to process SPT-based site characterization data for case histories in the NGL database, including the assignment of layer boundaries and soil properties within layers for use in model development. These steps include several new developments within the state-of-the-art in liquefaction evaluation, such as probabilistic estimates of *PI* and *FC* given a basic soil description.

#### 10.1 Assigning Observations to In Situ Tests

The first step in case history processing is to correlate the in situ test data (e.g., boreholes) in the database with nearby observations of liquefaction manifestation or no such manifestation. Observations of surface manifestation (or lack thereof) and site investigations are not necessarily co-located in the NGL database, so it is necessary to decide which observation should be associated with which borehole (i.e., what boreholes should be used in evaluating the soil layers that contributed to the surficial manifestation of liquefaction or lack thereof). Observations and boreholes (including their in situ tests) are associated through a link to a common site in the SQL data structure, but within a site there are often multiple observations and multiple boreholes. Furthermore, there are often "yes" and "no" observations of manifestations within the same site for the same earthquake. To make initial assignments of observations to boreholes, we developed the following algorithm using Python code in Jupyter Notebooks.

- 1. Select a site and identify all the boreholes and observations that are associated with that site.
- 2. Compile the latitude and longitude values for the boreholes and observations and compute an array containing the distance in meters between every observation and borehole at the site.
- 3. Separate the observations by event (some sites have observations from more than one earthquake event).
- 4. Assign the closest borehole to each observation for each event so that every observation has a borehole assigned to it.

The above four steps comprise an initial automated process to make these assignments, which is followed by a human review by SMT members examining each test-observation pair. To

conduct the review, the SMT developed a Jupyter notebook to visualize and summarize the available data for each site and event combination. A screenshot of the notebook is shown in Figure 10-1. Red markers indicate "yes" manifestation cases, black markers represent "no" manifestation, and green markers are locations of boreholes with SPT measurements. When a manifestation observation and borehole are co-located, the green pins are obscured, and a black or red circle is drawn around the pins to indicate co-location. The purpose of this review was to:

- 1) Confirm the appropriate assignments of "yes manifestation" and "no manifestation" to individual boreholes or groups of boreholes when more than one borehole could be reasonably assigned to the same field observation.
- 2) Identify and exclude case histories where the distance between a borehole and an observation of "yes manifestation" or "no manifestation" is too great to reasonably adopt (despite being the closest borehole identified by the initial algorithm). This evaluation is dependent on the site geology and the type and spatial distribution of field observations, and there is no single cutoff distance that is appropriate in every situation. For example:
  - a) A lateral spread feature extending over an area of many square meters is represented in the NGL database by a single latitude/longitude coordinate, usually near the center. The feature may contain several boreholes within its lateral extent, but the distance between the center point and the boreholes could be several meters. In this case, the appropriate maximum acceptable distance between an observation and a borehole may be greater than in another case where only a single sand boil is observed.
  - b) In other cases, it is important to evaluate how close a borehole is to a "yes manifestation" observation and a "no manifestation" when there are multiple observations in a single site.
  - c) Some sites may have more variable conditions, and the appropriate maximum acceptable distance between an observation and a borehole may be less than what is considered acceptable at a site where the soil profiles are more constant over horizontal distances. This evaluation is dependent on the site geology and available subsurface data.

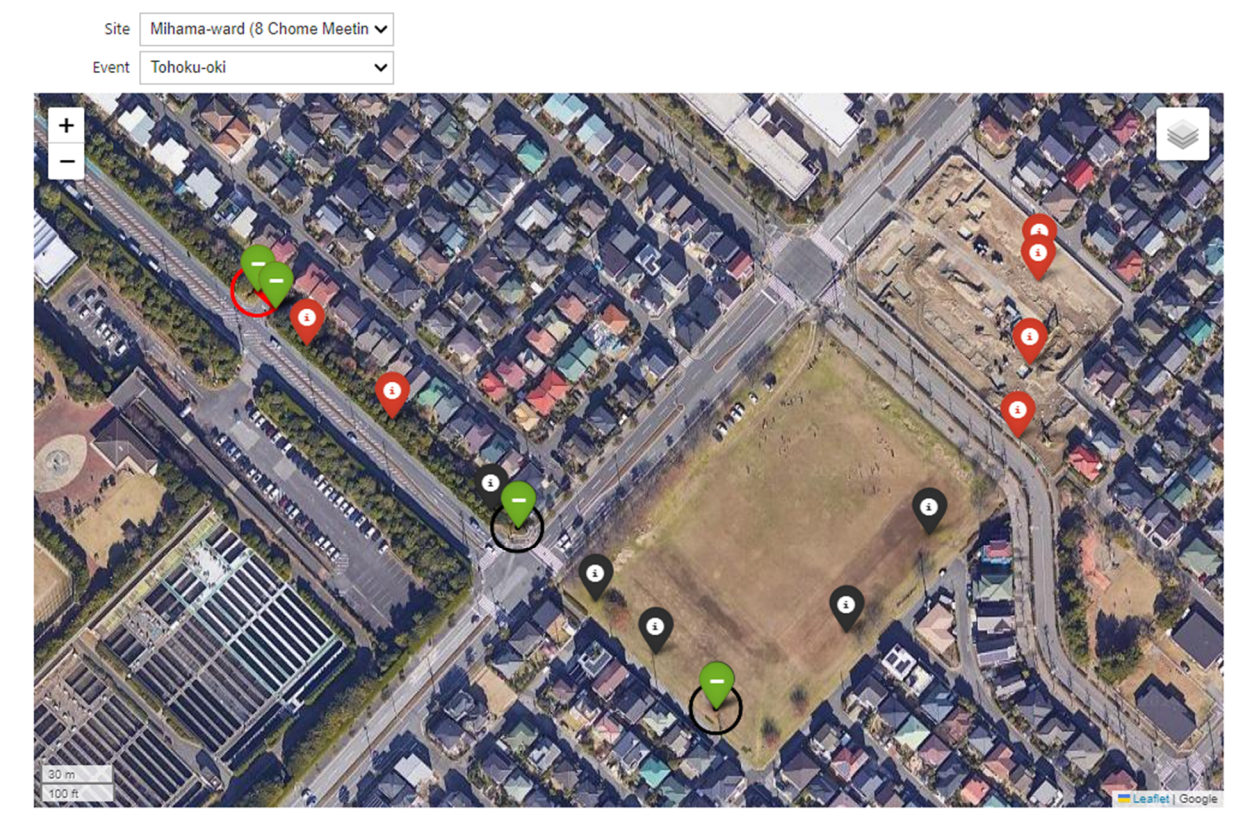


Figure 10-1 A screenshot of the Jupyter notebook that the SMT designed for reviews of individual case histories. Black markers represent observations of "no manifestation", red markers represent "yes manifestation", green markers represent boreholes, red/black lines connect boreholes and observations that the SMT grouped together, and red/black circles indicate a co-located borehole and observation pair. Case history: Mihama Ward, 2011 Tohoku earthquake.

- 3) Identify borehole data that should be disqualified for reasons not readily detected by the algorithms (e.g., insufficient detail or unreliable SPT hammer operations).
- 4) Identify case histories where the presence of nearby structures could potentially affect the manifestation of liquefaction.
- 5) Assign weights to boreholes when multiple boreholes are assigned to the same observation. In this manner, multiple boreholes may be paired with a single observation to form a single case history.

At least one member of the SMT, and often two or more, used this tool to review each case history that the algorithms initially identified. For this phase, only sites that were also reviewed as part of the CPT-based model development are included in our case history list, although an immediate task after submission of this report will be to broaden site selection by removing the co-located CPT requirement. This process yielded 119 case histories, each with a borehole associated with an observation of "yes" or "no" manifestation (the number of case histories when the co-located CPT requirement is dropped will exceed 430). Because over half of the field observations are co-located with a borehole, the median distance between site investigation locations and observations is less than a meter. The mean distance is 26m,

reflecting that some of the boreholes are tens of meters away from the observation's assigned location. This is not surprising for some large features, such as lateral spreads, which can span dozens of meters or more in length and width, but which are represented spatially in the database by a single pair of latitude and longitude coordinates.

#### 10.2 Layer Boundaries

After identifying the boreholes that are reasonably close to an observation, the next step is to identify soil layer boundaries within each borehole. The approach to identify layer boundaries in an SPT-based site characterization is necessarily different than the approach for CPT-based site characterization. For the CPT-based models, layer detection methods were automated using agglomerative clustering (Section 5.3 of the Task 7 report; Hudson et al., 2023a) because the process of performing a CPT sounding does not directly identify layer boundaries (e.g., there is no visual inspection of the soil, only digital measurements from the CPT cone). In the case of the SPT-based site characterization, boreholes are logged by an on-site professional who identifies transitions in soil type from samples, cuttings, and driller feedback as the drilling progresses. These identified transitions are captured in the NGL database in the stratigraphy (STRA) table. While borehole logs can miss some stratigraphic horizons and may not perfectly align with results of co-located CPT logs (e.g., Wang et al., 2019; Xie et al., 2024), the SMT decided to rely on these assigned boundaries as a starting point for our SPT-based model development.

One disadvantage to using STRA layers is that these layers tend to be large and ignore some of the nuanced differences captured by individual soil samples (SAMP) within each STRA layer. These soil samples are obtained during drilling for laboratory testing to measure fines content, plasticity index, particle gradation, and other soil properties. An alternative to using STRA layers would be to assign layers based on locations of SAMP entries, particularly those with SPT blow counts. However, this could lead to the opposite problem of having too many layers with only one data point per layer, resulting in potentially anomalous estimates of P[S] or P[T|S] within a layer. Furthermore, field geologists/engineers often log stratigraphic boundaries based on feedback from drill rig operators when a new layer is encountered, which may not align well with sampling locations.

We reviewed the stratigraphy information logged in each boring alongside the observed blow counts and sample descriptions (discussed in Section 10.3) and made our own judgment calls regarding appropriate locations of layer boundaries. The SMT developed a Jupyter notebook tool that facilitated feedback, such as recommending alternative layer boundaries, adjusting assumed *FC* and *PI* values, and noting layers with little data and a high level of uncertainty, as needed. Figure 10-2 shows a screenshot of this tool for a single case history. This review process is currently ongoing. This work was performed on a boring-by-boring basis rather than using multiple boring logs at a site to make a more holistic assessment of site stratigraphy. Our motivations were (1) adjacent borings at a site may not be associated with the same observation (e.g., one boring might be a "no" and the other a "yes" with respect to surface evidence of liquefaction, (2) borings are often spaced at a large enough distance that blow counts are not expected to be correlated within a layer, and (3) we did not have adequate time as of the writing of this report to perform a thorough review of all of the site investigations at

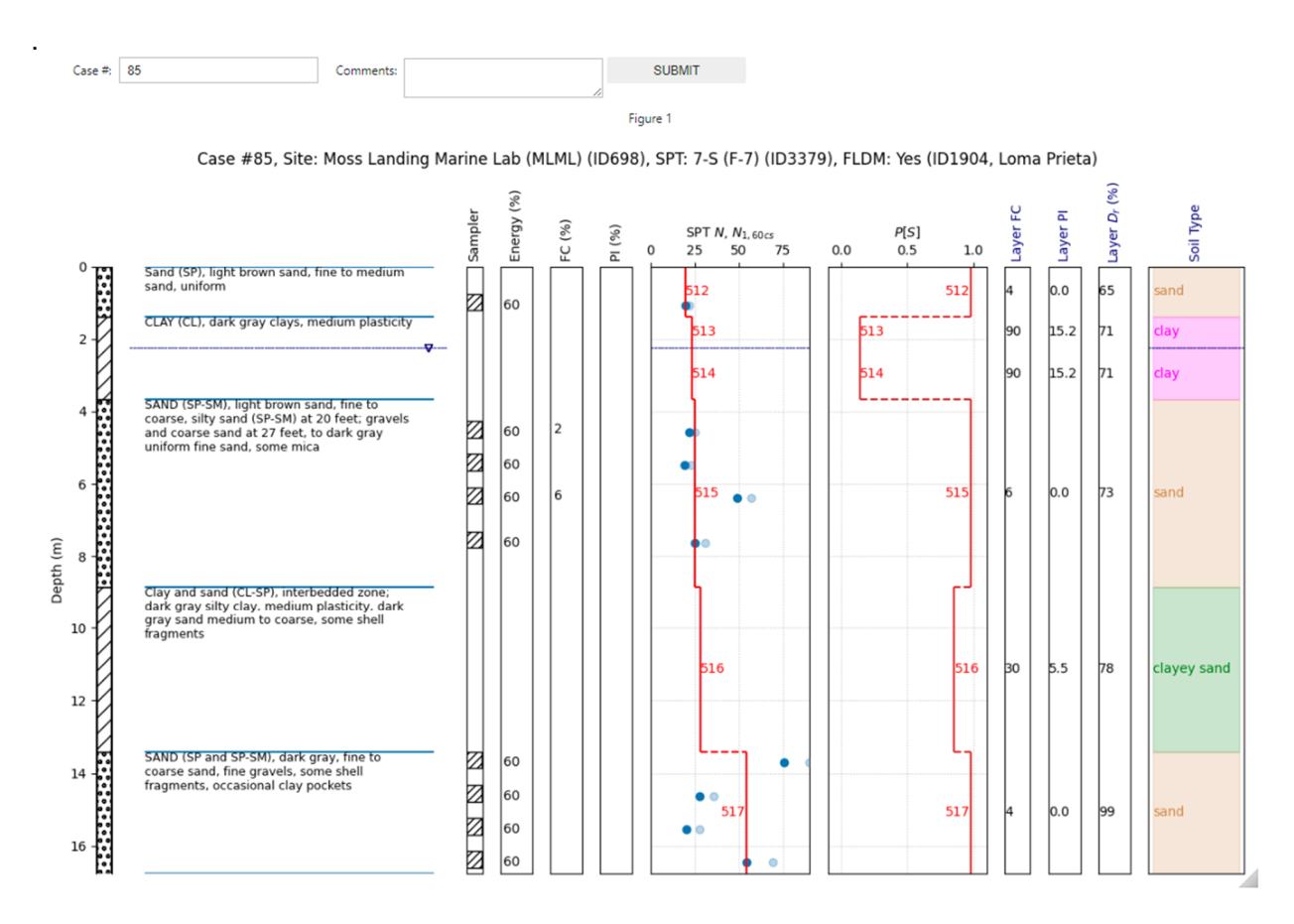


Figure 10-2 A screenshot of the Jupyter notebook that the SMT designed for reviews of layer boundaries and assigned layer properties for individual case histories.

each site. In future work, we plan to evaluate each site more thoroughly with respect to the position of adjacent borings, particularly in cases where SPT blow counts were not measured in a specific stratum

#### 10.3 <u>Assigning Layer Properties</u>

After identifying layer boundaries, the next step is to characterize each soil layer's strength, plasticity, and other characteristics relevant to liquefaction evaluation. We developed a number of different attributes for each layer in the profiles. Some attributes were computed directly from the SPT data, while others were assigned as representative values based on integration of several data sources. Section 10.3.1 describes how FC and plasticity (i.e., PI) are assigned. Section 10.3.2 outlines the process for normalizing measured SPT blow counts (N) to account for variations in overburden stress, energy, and fines content ( $N_{1,60cs}$ ), and for assigning representative normalized values to each layer.

Because SPT data is collected at discrete intervals with the potential for some soil layers to have no samples or SPT N values, the following sections outline how the SMT assigned representative values of FC, PI, and  $N_{1,60cs}$  for two scenarios: (i) where at least one measurement is available within a STRA layer, and (ii) where no measurements are available within a STRA layer. A list of attributes computed for the SPT-based case histories is provided in Appendix A.

#### 10.3.1 Estimation of **PI** and **FC**

Two important soil characteristics that are needed from SPT-based site characterization for model development are plasticity index, PI, and fines content, FC. As discussed later in Section 11.1, the P[S] depends on PI and, as discussed in Section 10.3.2, the normalized blow count,  $N_{1,60cs}$ , requires an estimate of FC. Thus, the SMT developed an objective process to assign PI and FC to each layer in our case history database.

#### 10.3.1.1 Representative PI and FC based on measurements

Where possible, PI and FC were obtained from measurements within each layer. In the cases where multiple samples within a layer had measured PI and FC values, the medians of all measured PI and FC values within a layer were assigned as representative values for the layer. The median is selected so that the value used is from a sample in the measured samples rather than an averaging of samples in the layer and not correlating to any one measurement. Additionally, the uncertainty on each of these values was quantified by combining two statistically independent variances: measurement error and spatial variability. The measurement error was taken as the COV reported in Table 5 of Phoon and Kulhawy (1999) for PI (0.24). That COV was converted to measurement error standard deviation for PI ( $\sigma_{PI,meas}$ ) in Eq. (10-1):

$$\sigma_{PI,meas} = COV_{PI} \cdot PI \tag{10-1}$$

Next, the within-layer dispersion of PI was estimated by examining the variance of PI within layers that have more than one PI measurement. First, the standard deviation was computed using the approximations given by Burrington and May (1970) and then squared to obtain the variance. The distribution of within-layer variance is shown in Figure 10-3. The within-layer variance,  $\sigma^2_{PI,spatial}$ , was taken as the mean of that distribution, which had a value of 81.9 with PI expressed in percent. The combined PI variance was then computed as:

$$\sigma_{PI}^2 = \sigma_{PI,meas}^2 + \sigma_{PI,spatial}^2 \tag{10-2}$$

The following is applied for layers that contain just one *PI* measurement:

- 1.  $\sigma_{PI,meas}$  is assigned using Eq. (10-1) with the measured PI and the COV from Phoon and Kulhawy (1999)
- 2. The median value of  $\sigma_{PI,spatial}^2$  from Figure 10-3 is used
- 3. The total variance,  $\sigma_{PI}^2$  is computed using Eq. (10-2).

For layers that have more than one PI measurement, the same procedure is applied except that the median PI value from the layer is used in Eq. (10-1) to compute  $\sigma_{PI,meas}$ .

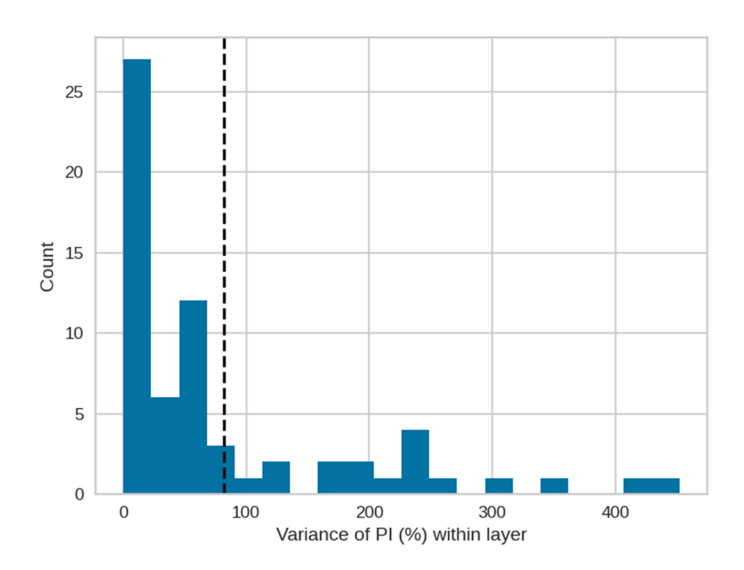


Figure 10-3 Histogram of the variance of *PI* within layers. The mean is represented by the dashed vertical black line. The dataset used to compute these variances includes *PI* measurements from 65 layers that have more than one Atterberg limit test performed within the STRA table defined layer.

The *FC* uncertainty does not consider any measurement error because Phoon and Kulhawy (1999) did not provide uncertainty for *FC*, likely because it is a laboratory test with small variance. Spatial uncertainty is considered in the same manner as for *PI*. The distribution of *FC* within-layer variance is presented in Figure 10-4. The mean of that distribution, with *FC* expressed in percent, is taken as  $\sigma_{FC.meas}^2 = 381$ .

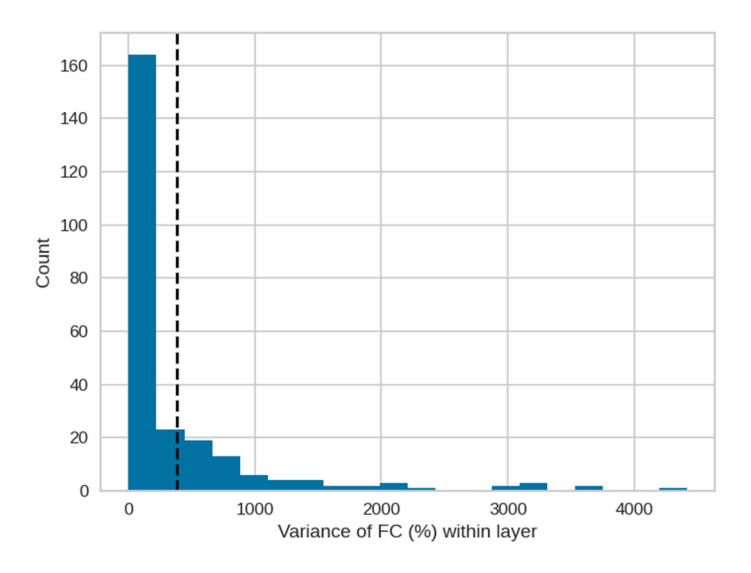


Figure 10-4 Histogram of the variance of FC within layers. The mean is represented by the dashed vertical black line. The dataset used to compute these variances includes FC measurements from 287 layers that have more than one grain size distribution test performed within the STRA table defined layer.

#### 10.3.1.2 Representative PI and FC without measurements

In an SPT-based site characterization, soil samples are collected at discrete intervals with the potential for some soil layers to have no samples. Thus, not all STRA layers contain *PI* and *FC* values derived from laboratory testing, but they do have visual manual classification information about the soil within the layer. Therefore, the SMT developed an approach to infer *PI* and *FC* from text descriptions.

After reviewing stratigraphic text descriptions of STRA layers and samples (from the SAMP table) in the NGL database, we assigned one of 11 basic soil type labels as follows:

- Gravel
- Sand
- Silty Sand
- Clayey Sand
- Silt
- Sandy Silt
- Clayey Silt
- Clay
- Sandy Clay
- Silty Clay
- Organic

These basic soil type labels are used at two stages. Initially they are used for STRA layers or samples for which *PI* and *FC* data are available to develop predictive relations. Subsequently, they are used to assign representative values to STRA layers for which no tests are available.

In the initial stage, SMT members checked the value of *FC* (if it was measured) against the text descriptions and relied on the *FC* of each sample to ultimately assign the soil type as needed. For example, a STRA layer may have been described as "sandy silt" in the field, but the laboratory specimen from that layer may have *FC* less than 50%, which would indicate that the soil is predominantly composed of coarse-grained soils and should instead be called "silty sand". Our opinion is that the best practice for constructing boring logs is to revise text descriptions to be consistent with laboratory test data, but this was not always done for the boring logs in the database.

After making these basic soil type assignments to all samples with measured *PI* or *FC* values, the SMT developed distributions of *PI* and *FC* within each of these basic soil type labels. Figure 10-5 and Figure 10-6 show these distributions. The blue shaded areas represent approximate histograms of the data, in addition to the box and whisker plots. Medians are represented by an orange bar, and means are reported at the top of each plot. As expected, the mean and median *PI* for "sand" is zero, while the mean and median *PI* values are higher for predominantly fine-grained soils (e.g., "clay" or "silt").

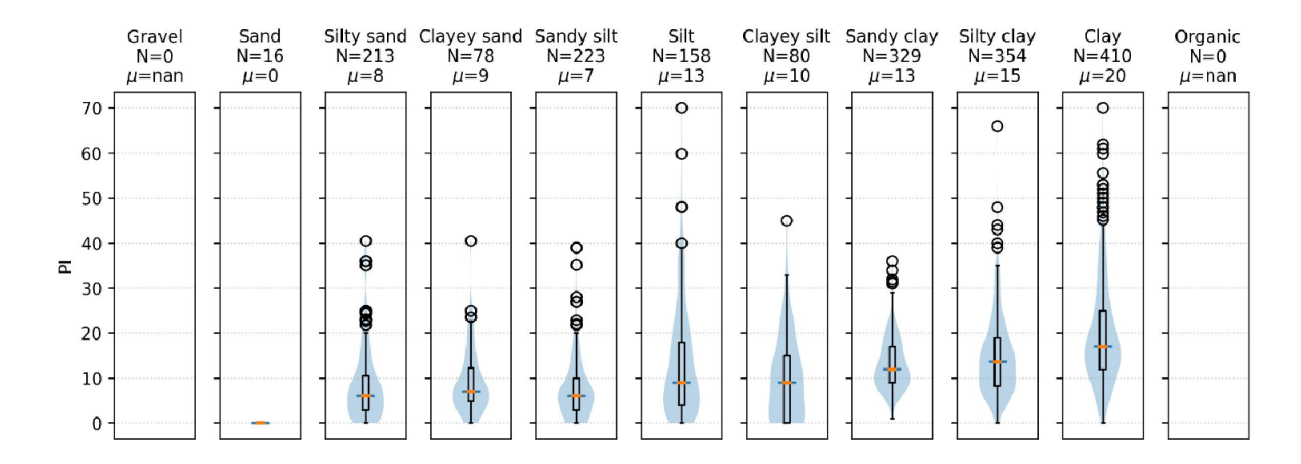


Figure 10-5 Distributions of *PI* within each soil type group. The blue shaded area represents an approximate histogram of the data, with box and whisker plots in black. Medians are represented by an orange bar, and means are reported at the top of each plot.

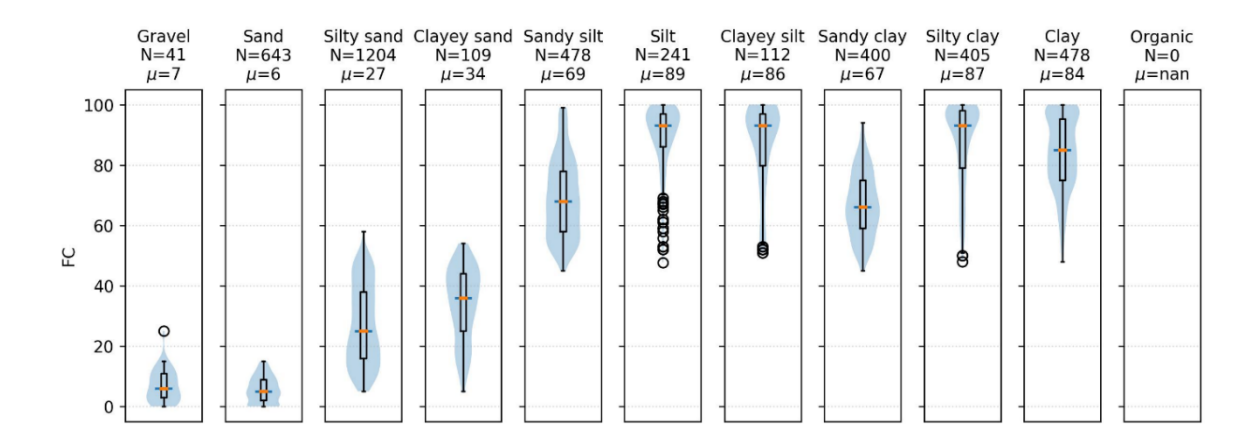


Figure 10-6 Distributions of *FC* within each soil type group. The blue shaded area represents an approximate histogram of the data, with box and whisker plots in black. Medians are represented by an orange bar, and means are reported at the top of each plot.

To simplify the groupings and to increase the number of data points within some poorly represented soil types, some of the basic soil types were grouped together based on similar *PI* or *FC* distributions. For example, "silty sand", "clayey sand", and "sandy silt" had nearly identical *PI* distributions. Thus, the original 11 soil type labels for *PI* distributions were redefined into soil type groups as outlined in Table 10-1.

To capture the uncertainty in the *PI* and *FC* estimates within these layers, the SMT characterized the distributions of *PI* within each soil type group using a mean and standard deviation. However, the distributions for *PI* were skewed such that a normal distribution did not fit well. Thus, we performed Box-Cox transformations (Box & Cox, 1964) as defined in

Table 10-1 Soil type groups for PI and FC distributions

Soil Type Groups for PI Distributions	Soil Type Groups for FC Distributions
Gravel or Sand	Gravel or Sand
Silty Sand, Clayey Sand, or Sandy Silt	Silty Sand
Sandy Clay	Clayey Sand
Silt or Clayey Silt	Silt
Silty Clay	Sandy Silt
Clay	Clayey Silt
Organic	Clay
	Sandy Clay
	Silty Clay
	Organic

Eq. (10-3) within each soil type group to obtain values of  $\lambda$ , mean  $\widehat{PI}$ , and standard deviation of  $\widehat{PI}$ .

$$\widehat{PI} = \frac{PI^{\lambda_{PI}} - 1}{\lambda_{PI}} \tag{10-3}$$

The Box-Cox transformed distributions are shown in Figure 10-7, and Table 10-2 summarizes the  $\lambda_{Pl}$ , mean  $\widehat{Pl}$ , and standard deviation of  $\widehat{Pl}$  from the Box-Cox transformation for each soil type group. Note that for some soil groups (e.g., "gravel" and "organic") we had no soils with those descriptions that also had Pl measurements. The SMT assumed that the representative Pl values for "gravel" and "organic" were 0 and 50, respectively. Also, for the "sand" group, all of the Pl measurements were 0 (i.e., non-plastic). In this case, the SMT assumed that the representative Pl value for "sand" was 0.

We repeated the Box-Cox transformation process using FC data to obtain estimates of  $\lambda_{FC}$ , mean  $\widehat{FC}$ , and standard deviation of  $\widehat{FC}$ , where  $\widehat{FC}$  is defined as

$$\widehat{FC} = \frac{FC^{\lambda_{FC}} - 1}{\lambda_{FC}} \tag{10-4}$$

Figure 10-8 shows the Box-Cox transformed distributions for  $\widehat{FC}$  and Table 10-3 summarizes the resulting parameters  $\lambda_{FC}$ , mean  $\widehat{FC}$ , and standard deviation of  $\widehat{FC}$ . There were no measured FC values in layers labeled "organic", and thus the SMT assumed that the representative FC value was 80.

There is some inherent uncertainty in the assignment of basic soil type labels for each STRA layer. In some cases, STRA text fields do not have sufficient detail. For example, a layer may be described as "sand with fines," which does not have the required level of detail to distinguish "clayey sand," "silty sand," and "sand." In these cases, we check first for a measured *FC* value to establish whether the soil should be called "sand" (i.e., *FC* less than 50%). If there is no measured *FC* value within the layer to help guide the assignment of the soil type label, then "silty sand" is assigned. In other cases, there may be multiple SAMP within a STRA

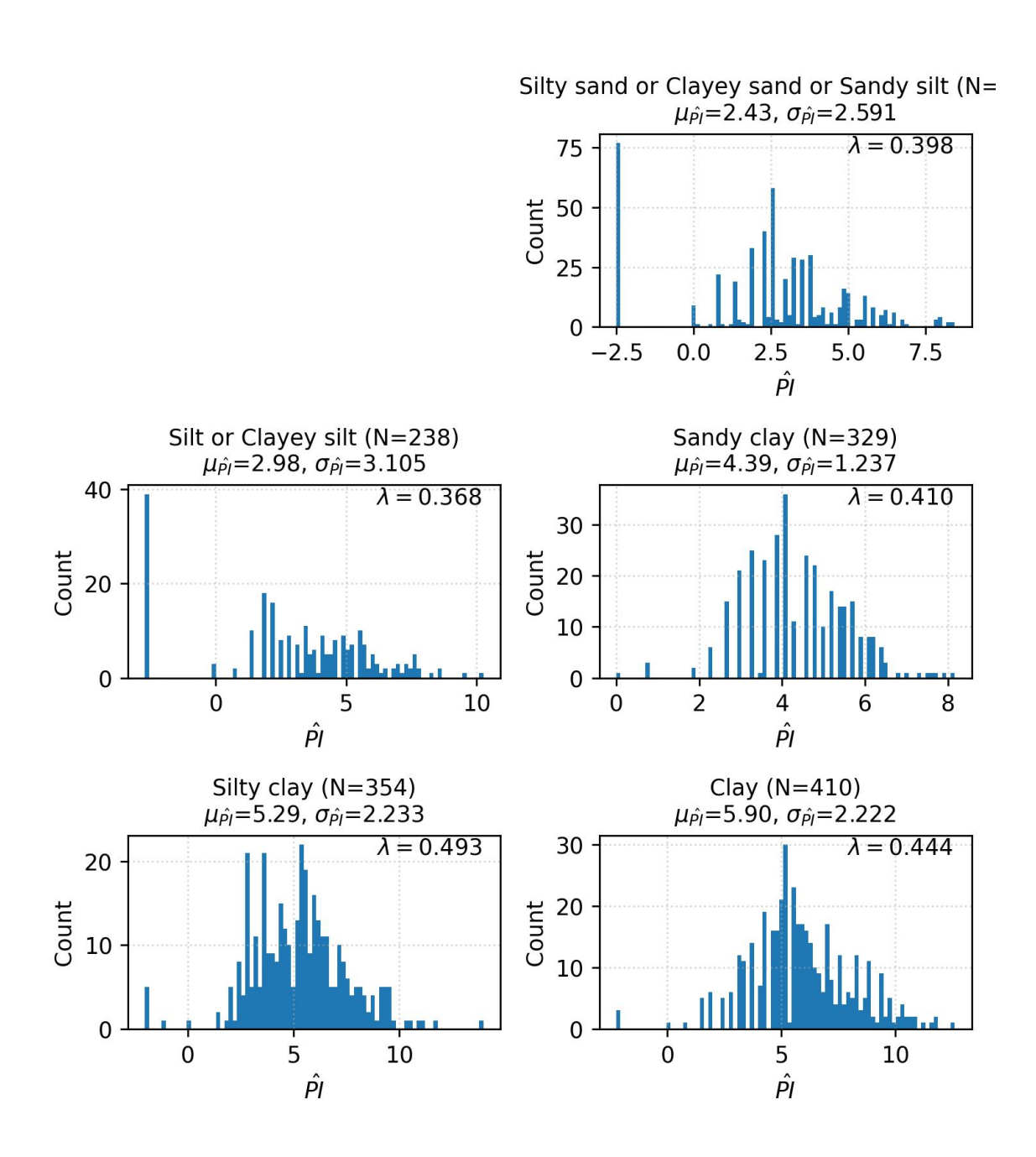


Figure 10-7 Box-Cox transformations for PI in each soil type group.

Table 10-2  $\lambda_{Pl}$ , mean  $\widehat{Pl}$ , standard deviation of  $\widehat{Pl}$ , and mean Pl from Box-Cox transformation for each soil type group

Soil Type Group	λρι	ΡĨ	$\sigma_{\widehat{Pl}}$	PI
Gravel or Sand	1	-1	1	0
Silty sand or Clayey sand or Sandy silt	0.3980	2.43	2.591	5.5
Silt or Clayey silt	0.3682	2.98	3.105	7.5
Sandy clay	0.4102	4.39	1.237	12.3
Silty clay	0.4935	5.29	2.233	13.5
Clay	0.4438	5.90	2.222	18.2
Organic	1	49	1	50
Fill	1	3	6	4

layer that have conflicting descriptions. For example, a layer may have three samples with soil type descriptions (SAMP\_DESC) of "silty sand", "silty sand", and "sand". In these cases, the representative soil type label for the STRA layer is assigned as the mode of the individual SAMP soil types, which in this example would be "silty sand." Results are summarized in a pickle file format (with a .pkl file extension) containing the SMT's processed case history data (Appendix A). The individual soil types of the SAMPs within a layer are listed in the column called "soil\_type\_all", whereas the representative soil type of the STRA layer is in the column called "soil\_type." This allows the SMT to track these details when reviewing layer boundaries and representative soil characteristics.

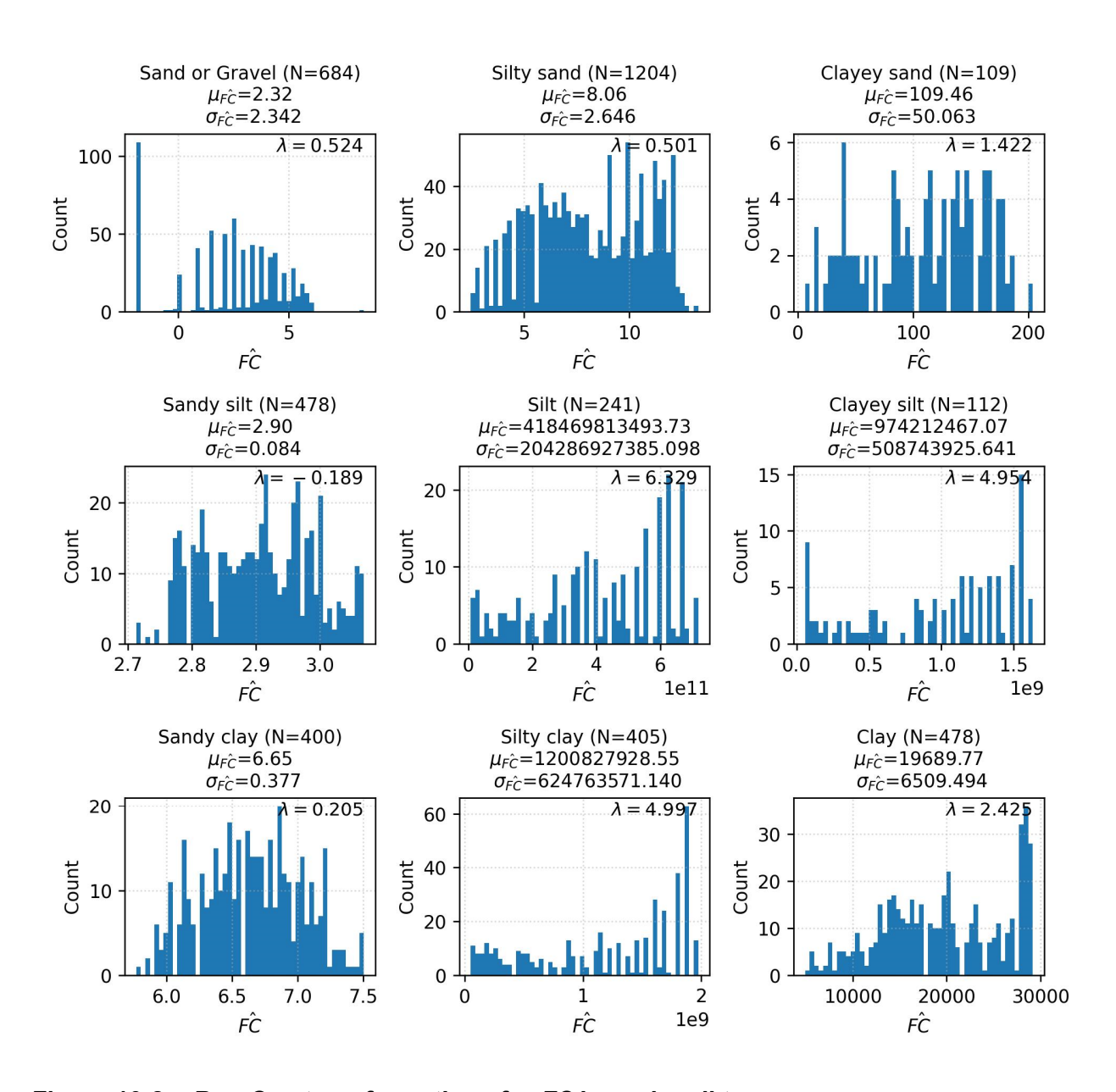


Figure 10-8 Box-Cox transformations for FC in each soil type group.

Table 10-3  $\lambda_{FC}$ , Mean  $\widehat{FC}$ , and standard deviation of  $\widehat{FC}$  from Box-Cox transformation and mean FC for each soil type group

Soil Type Group	$\lambda_{FC}$	FC	$\sigma_{\widehat{FC}}$	FC (%)
Gravel or Sand	0.5243	2.32	2.342	4.6
Silty sand	0.5012	8.06	2.646	25.2
Clayey sand	1.4222	109.5	50.063	34.9
Sandy silt	-0.1893	2.9	0.084	67.7
Silt	6.3291	4.18E11	2.04E11	91.8
Clayey silt	4.9537	9.74E8	5.09E8	90.1
Sandy clay	0.2052	6.65	0.377	66.3
Silty clay	4.9972	1.2E9	6.24E8	90.5
Clay	2.4247	1.9E4	6.5E3	85.0
Organic	1	79	30	80
Fill	1	19	30	20

#### 10.3.2 Penetration Resistance and Stress Normalization

The decision to use STRA defined layer boundaries for SPT-based site characterization data means that there are many layers with more than one measured blow count (*N*) and some layers without any *N* values. For use in the profile-based model development, each layer needs to have an *N* value for calculation of the cyclic resistance of the soil, therefore an automatic workflow is established to make assignments of the representative *N* value within each layer.

If a layer has one measured N value between the top and bottom of the layer, then that value is used as the representative value. If a layer has multiple N values, the median of the measured N values within the layer is taken as the representative value. If a layer does not have any N values, then the closest N value in the boring is assigned as representative of that layer. This can be problematic and every instance where this occurs will be carefully reviewed (Section 10.2). For instances where a layer without an N value is deemed inconsequential from the perspective of profile manifestation (e.g., a thin clay layer), then the layer is excluded by setting all of the probabilities (defined in Chapter 11) to zero so that it does not influence the profile-based calculations.

For reasons discussed in Section 12.1, SPT blow counts carry significant measurement error compared with CPT tip resistance. To account for this error, the measurement uncertainty for N is approximated using a COV of 50%, which is between the recommended 54% for sand and 44% for clay from Phoon and Kulhawy (1999). Spatial uncertainties are considered in the same manner as described in Section 10.3.1 for PI and FC. The spatial variance for N,  $\sigma_{N,spatial}^2$ , for every layer with more than one N measurement is shown in Figure 10-9. The mean value of that distribution ( $\sigma_{N,spatial}^2$ =71.2) is used as the spatial variance where there is only one N value within a layer. For layers with more than one, the variance is computed using the ranged-based method of Burrington and May (1970). For layers with no measured N values, the  $\sigma_{N,spatial}^2$  value is multiplied by 1.5 to account for increased uncertainty in the true N value.

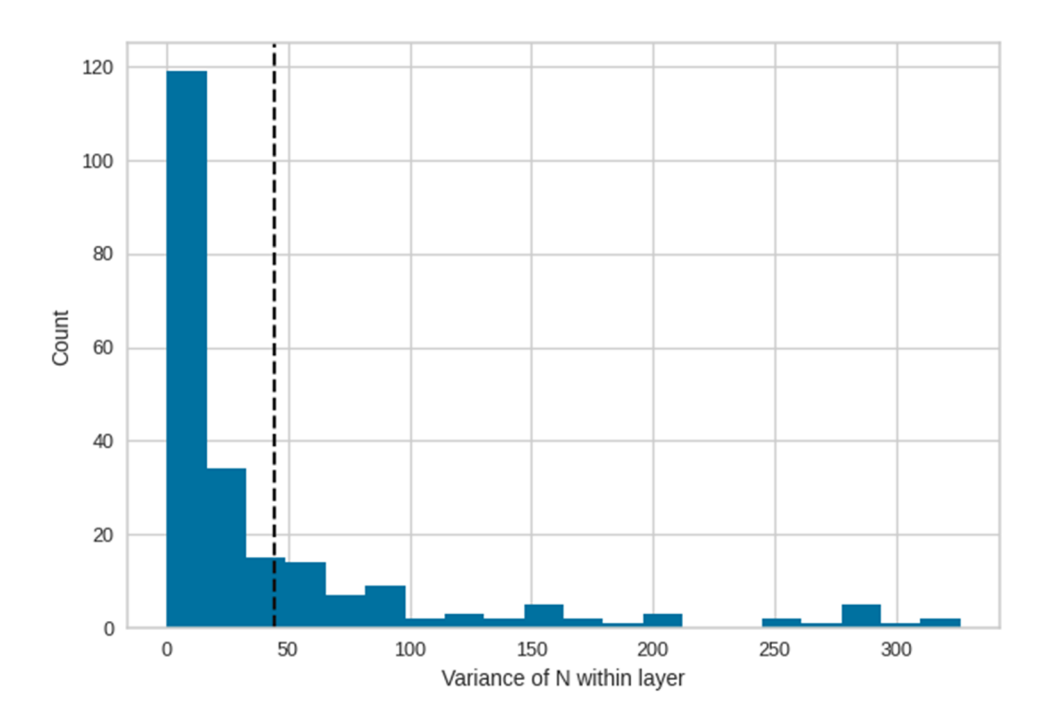


Figure 10-9 Histogram of the variance of N within layers. The mean is represented by the dashed vertical black line. The dataset used to compute these variances includes N from 227 layers that have more than one SPT performed within a single STRA defined layer.

SPT N values are corrected for energy and stress. First, N is converted to a normalized blow count associated with 60% energy ( $N_{60}$ ) using the hammer energy ( $ER_m$ ) and the relationship shown in Eq. (10-5) (Seed et al., 1985), where  $C_E$  is the ratio of  $ER_m$  over 60%. Where possible,  $C_E$  was computed using  $ER_m$  reported by the original author of the study as documented in the NGL database. If  $ER_m$  was not reported by the author, then  $C_E$  was assigned based on the hammer type if sufficient information was given. For example, if the hammer type is "safety", "automatic trip", or "donut" type, it is given  $C_E = 0.95$ , 1.0, and 0.7, respectively. These are approximately mean  $C_E$  values for these hammer types as reported by Youd et al. (2001). If the hammer type is not reported, then the date of the exploration is used to estimate  $C_E$ : if the exploration occurred before the year 2000, it is assigned  $C_E = 1.0$  (i.e.,  $ER_m = 60\%$ ), whereas if it was 2000 or later,  $C_E = 1.33$ . If the date is unknown,  $C_E = 1.17$ .

$$N_{60} = N \frac{ER_m}{60\%} = NC_E \tag{10-5}$$

For stress normalization, an estimate of the unit weight profile is created using the specific gravity ( $G_s$ ) and water content ( $w_c$ ) measurements in the boring. If one or neither of these values are present at a particular depth range or in nearby borings, then the  $G_s$  and  $w_c$  are assumed to be 2.7 and 35%, respectively. Assuming saturation (S=1) beneath the ground water table, the unit weight is computed as

$$\gamma = \frac{\gamma_w(e + G_s)}{1 + e} \tag{10-6}$$

where e is the void ratio equal to  $G_s(w_c/100\%)$  and  $\gamma_w = 9.81$ kN/m³. Assuming S=0 above the groundwater table, the unit weight is computed as

$$\gamma = \frac{\gamma_w(G_S)}{1+e} \tag{10-7}$$

If there is an associated groundwater table depth in the WATR table assigned to the boring, we select that value for case history processing. If there is no associated entry in the WATR table assigned to the boring, we assign the closest groundwater table depth at any in situ test at the site (e.g., another borehole or a nearby CPT). These quantities are all used to compute the total and effective stress profile for the boring. The stresses are used to normalize *N* using the equations recommended in Idriss and Boulanger (2008):

$$(N_1)_{60} = C_N \cdot N_{60} \tag{10-8}$$

$$C_N = \left(\frac{P_a}{\sigma_v'}\right)^m \le 1.7 \tag{10-9}$$

$$m = 0.784 - 0.0768\sqrt{(N_1)_{60cs}} ag{10-10}$$

where  $p_a$  is atmospheric pressure (i.e., 1 atm = 101.325 kPa). Normalized, clean sand equivalent values ( $N_{1,60cs}$ ) are computed as

$$(N_1)_{60cs} = (N_1)_{60} + \Delta(N_1)_{60cs}$$
(10-11)

$$\Delta(N_1)_{60cs} = \exp\left(1.63 + \frac{9.7}{FC + 0.01} - \left(\frac{15.7}{FC + 0.01}\right)^2\right)$$
(10-12)

where FC is fines content in percent (Boulanger and Idriss, 2014).

A list of attributes computed for the SPT-based site characterization data is provided in Appendix A, including layer depth, layer thickness, representative SPT N value, N variance, representative overburden- and fines-corrected N value ( $N_{1,60cs}$ ), soil type, PI, PI variance, FC, FC variance, vertical effective and total stress, groundwater table depth, CSR, MSF, and  $K_{\sigma}$ . These attributes are computed in Python and stored in a pickle file format (with a .pkl file extension) that is well suited to being read into a Pandas dataframe. We will publish these data as part of this project to facilitate use by other model development teams.

## 10.3.3 Cyclic Stress Ratio

We compute seismic demands on soil layers in the form of a cyclic stress ratio,  $CSR_{M7.5,1atm}$  in the same manner as for the CPT-based models in the Task 7 report [Eq. (5-27) through Eq. (5-35) in Section 5.4.3].  $CSR_{M7.5,1atm}$  is computed for a given earthquake event and ground motion that has been associated with an observation of surface manifestation (or lack thereof) at or near the location of the borehole. Some locations have been shaken by multiple earthquakes; in which case the borehole data is repeated in the summary pkl file (see Appendix A for full list of quantities in the pkl file).

As was the case for the CPT-based models,  $CSR_{M7.5,1atm}$  values computed at the center of each layer are taken to be representative of the layer, and  $CSR_{M7.5,1atm}$  is computed using the PGA estimates from the Kriging approach outlined in Section 5.2 of the Task 7 report, where possible. For our fully reviewed dataset, 117 of the PGA values were obtained from Kriging and 2 were not obtained from Kriging. In the latter case, we relied on legacy estimates of PGA, which typically used best estimates from available ground motion models.

#### 11 SPT-BASED MODELS

As described in Chapter 4 of the Task 7 report, the necessary components of the SMT's conditional probabilistic approach include estimates of P[S], P[T] = P[T|S]\*P[S], P[M|T], and P[M|NT]. The following sections outline the preliminary approaches adopted by the SMT to estimate these probabilities using SPT-based site characterization data.

Section 11.1 presents the SMT's selected model to estimate the probability of susceptibility P[S] based on existing models from literature. Section 11.2 describes a model for triggering that is derived from laboratory cyclic test results as given in Section 6.2 of the Task 7 report. Section 11.3 provides some comparisons to show compatibility with existing legacy models and the SMT's CPT-based models (Task 7 report). Finally, Section 11.4 presents a framework to obtain a model for manifestation based on SPT-based site characterization data using a similar profile-based regression framework described in Section 4.4.3 of the Task 7 report.

## 11.1 Probability of Susceptibility, P[S]

Based on the definition of susceptibility in Section 2.1.1 of the Task 7 report, our susceptibility model considers a soil's mineral composition as inferred from PI (or  $I_c$  for CPT-based models), and excludes non-compositional factors such as state, saturation, and manifestation potential. Note that in our approach, saturation is considered as part of the P[T] relationship, as discussed in Section 4.4.1 of the Task 7 report. The following section outlines a set of P[S] models we developed based on PI.

#### 11.1.1 P[*S*] as a Function of *PI*

Our susceptibility model is probabilistic to reflect natural variability of soil behavior and to quantify epistemic uncertainty. Following a public workshop on the topic (Stuedlein et al., 2023), a framework for creating new susceptibility models using the laboratory component of the NGL database was formulated. However, the implementation of this framework is in its beginning stages and has not yet been adopted by the broader liquefaction research community. Therefore, we developed preliminary P[S] models based on legacy deterministic susceptibility models, namely Bray and Sancio (2006) and Boulanger and Idriss (2006). We use the following equation, which is a logistic function approximation of a cumulative normal distribution function:

$$P[S] = 1 - \frac{1}{1 + exp\left(-\frac{1.702}{\sigma_m} * (PI - x_m)\right)}$$
(11-1)

where  $x_m$  and  $\sigma_m$  are moments of a normal distribution. We digitized data from plots given by Bray and Sancio (2006) and Boulanger and Idriss (2006) containing pairs of PI and susceptibility labels [i.e., "susceptible", "marginally susceptible", and "not susceptible" for Bray and Sancio (2006), "sand-like", "intermediate", and "clay-like" for Boulanger and Idriss (2006)]. We then assigned P[S] values of 1.0, 0.5, and 0.0 for data points with "susceptible", "marginally susceptible", and "not susceptible" labels, respectively, assuming "sand-like" = "susceptible", "intermediate" = "marginally susceptible", and "clay-like" = "not susceptible". Figure 11-1 shows those data points and probability density functions for each susceptibility label. We then fit Eq. (11-1) to the data ("data fit" in the figure). Huang (2008) previously developed P[S] relationships for the Bray and Sancio (2006) and Boulanger and Idriss (2006)

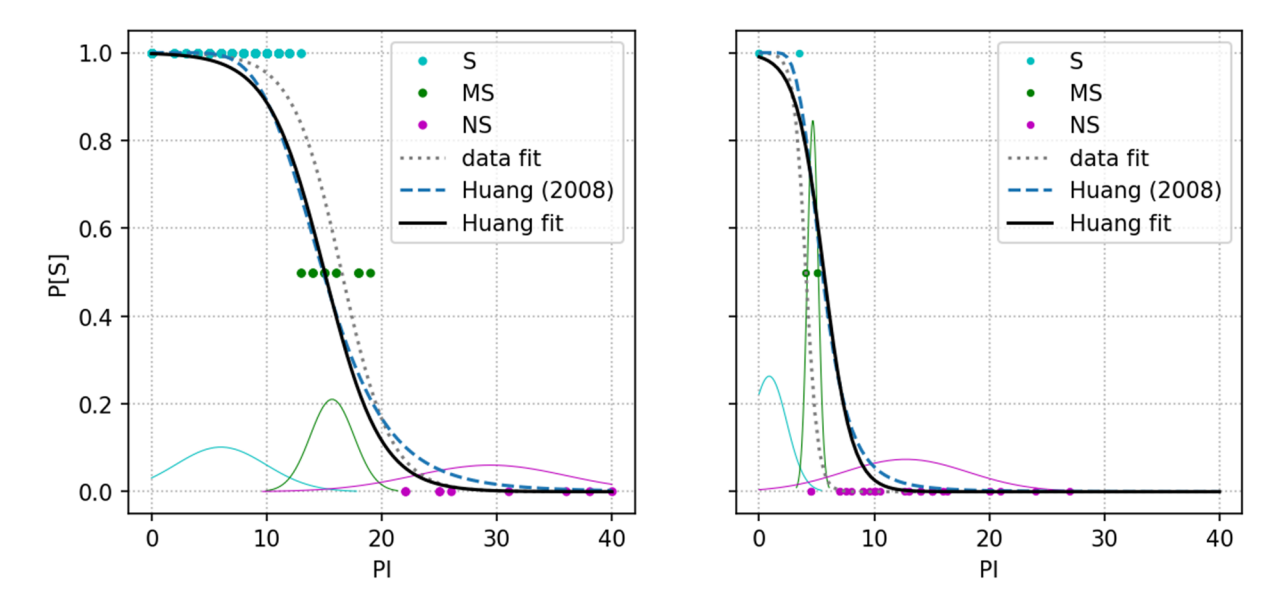


Figure 11-1 Digitized datapoints from (a) Bray and Sancio (2006) and (b) Boulanger and Idriss (2006) with susceptibility labels S = susceptible, MS = marginally susceptible, and NS = not susceptible. Thin lines represent probability density functions for each susceptibility label and the thick black lines represent the SMT's P[S] models as a function of PI using Eq. (11-1).

datasets that also incorporate some of the original authors' judgment and uncertainty in the measurement of PI. These P[S] relationships from Huang (2008) are also shown in Figure 11-1 for comparison. The SMT decided to use Huang's P[S] models, but to rewrite them in our preferred functional form (Eq. 11-1). The Huang (2008) models rewritten in our functional form are also shown in Figure 11-1 for comparison (labeled "Huang fit"). The coefficients  $x_m$  and  $\sigma_m$  for both models are summarized in Table 11-1.

The range of results in Figure 11-1 constitute a partial representation of epistemic uncertainty. We decided to treat this uncertainty using a logic tree approach to obtain PI-conditioned probabilities of susceptibility. We used equal weighting between the models because both models represent equally reasonable interpretations of available data. The dashed line in Figure 11-2 represents the average P[S] for each PI. This line was not considered to be suitable for application due to its irregular shape, so a fit using Eq. (11-1) was developed that produced the combined model shown in Figure 11-2, which has  $x_m = 10.34$  and  $\sigma_m = 4.651$ .

To incorporate the susceptibility model into the Bayesian inference framework utilized to obtain the manifestation model coefficients, a distribution function with a mean and standard deviation must be assigned to each model parameter (i.e.,  $x_m$  and  $\sigma_m$  for P[S]). The Bayesian prior distributions were assumed to be normal with the mean  $x_m$  and  $\sigma_m$  values defined by the combined SMT model values (Table 11-1). The uncertainty in  $x_m$  and  $\sigma_m$  was quantified by approximating the standard deviation of the  $x_m$  and  $\sigma_m$  values from the Bray and Sancio (2006) and Boulanger and Idriss (2006) models using the method by Burrington and May (1970), yielding 8.34 and 1.85, respectively.

Table 11-1 Coefficients in Eq. (11-1) for three P[S] models

Model	Xm	$\sigma_{m}$
Bray and Sancio (2006), modified from Huang (2008) interpretation	15.04	4.164
Boulanger and Idriss (2006), modified from Huang (2008) interpretation		2.071
Combined SMT model (this study)	10.34	4.651

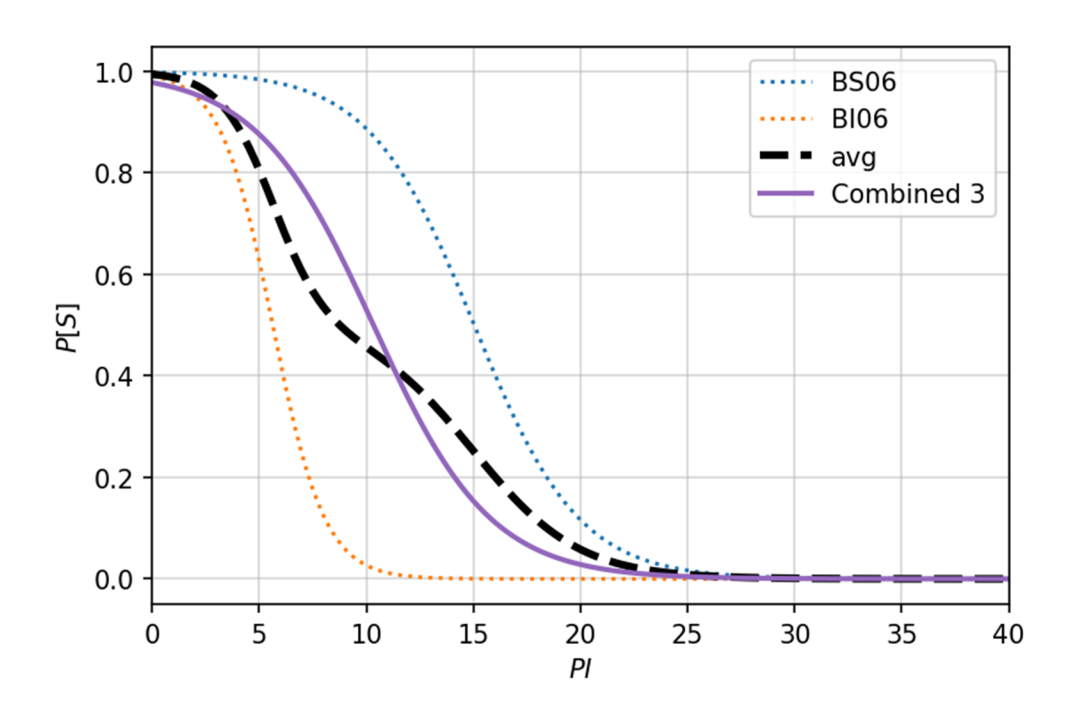


Figure 11-2 P[S] models based on Bray and Sancio (2006), Boulanger and Idriss (2006), and the SMT's combined model. The dashed line represents an average between the BS06 and Bl06 models.

#### 11.1.2 P[S] as a Function of Soil Description Alone

In the CPT-based model, CPT data was continuous throughout the soil profile and thus the  $I_{c}$ -based P[S] model (Section 6.1 of the Task 7 report) was applicable for all CPT soundings at all depths where data was available. However, in the case of boreholes, samples are taken at much more widely-spaced and discrete intervals, with the potential for some soil layers to lack samples. Therefore, some soil layers could be missing an estimate of PI due to (i) no samples taken within that layer, or (ii) soil specimens from available samples were not tested in the laboratory to measure PI. As a result, the SMT developed an alternative approach to assign reasonable values of P[S] to soil layers without measured PI values.

To assign P[S] for layers without PI measurements, we adopt the distribution of  $\widehat{PI}$  for each soil type using parameters defined in Table 10-2 and then compute P[S] as a function of  $\widehat{PI}$  using the combined model shown in Section 11.1.1. Table 11-2 summarizes the mean PI, standard

deviation of PI, and representative P[S] for a given soil type. The values of P[S] in this table were obtained by integrating the product of the PDF of the PI values in each bin (e.g., Figure 10-5 in Section 10.3.1.2) with the CDF of the SMT's combined P[S] model introduced in Section 11.1.1.

$$P[S] = \int_0^\infty f_{PI} \cdot F_{sus} dPI \tag{11-2}$$

where  $F_{sus}$  is the cumulative distribution function defined in Eq. (11-1) and  $f_{Pl}$  is the probability density function of PI for each soil type defined by the normal distribution:

$$f_{PI} = \frac{1}{\sigma_{PI}\sqrt{2\pi}}e^{-\frac{(PI - \mu_{PI})^2}{2\sigma_{PI}^2}}$$
(11-3)

where  $\mu_{Pl}$  and  $\sigma_{Pl}$  are the mean and standard deviation of Pl for each soil type, respectively. The integration was approximated as the following summation to solve numerically because there is no analytical solution to this convolution:

$$P[S] = \sum_{0}^{40} f_{PI}(PI) \cdot F_{sus}(PI)$$
 (11-4)

Table 11-2 Mean *PI*, standard deviation of *PI*, and associated P[*S*] from the combined SMT model for each soil type group

Soil Type Group		$\sigma_{Pl}$	P[S]
Gravel or Sand		0	0.985
Silty sand or Clayey sand or Sandy silt	5.5	5.933	0.563
Silt or Clayey silt	7.5	7.926	0.450
Sandy clay		2.719	0.358
Silty clay	13.5	4.505	0.311
Clay	18.2	4.694	0.117

Figure 11-3 compares the SMT's PI-based P[S] model with the P[S] estimates based on text descriptions assigned as described in Section 10.3.1.2. The data represented in this figure have measured PI values and soil type labels based on text descriptions as discussed in this section. The shaded areas show the relative distribution of PI values, centered vertically on the assigned value of P[S] based on the soil type group. The small vertical lines represent the median PI for that group. In general, the SMT's estimates of P[S] based on text descriptions are in good agreement with the PI-based P[S] values, with some uncertainty. This is expected, as the text descriptions are not perfectly mapped to values of PI and have some dispersion (as shown previously in Section 10.3.1.2)

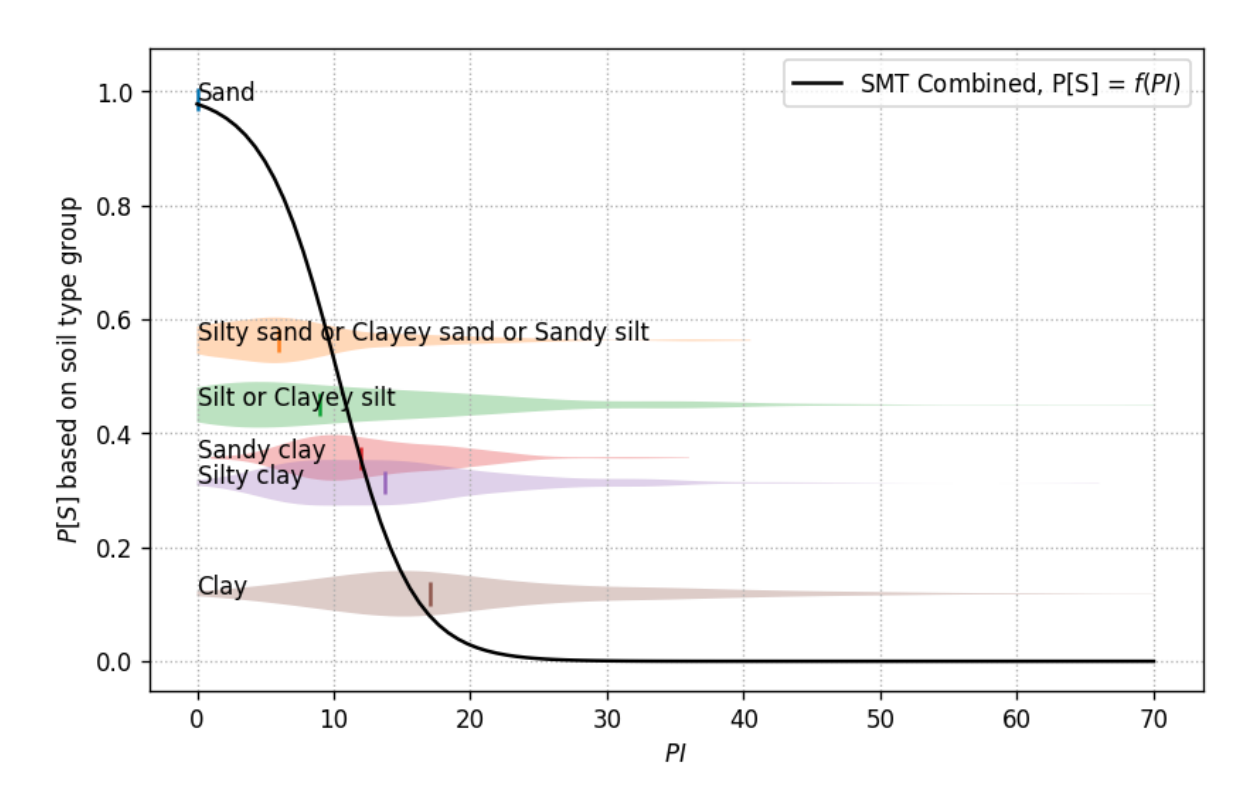


Figure 11-3 Comparison of the SMT's *PI*-based P[S] model with the SMT's P[S] estimates based on text descriptions. Shaded areas represent relative distributions of *PI* in each soil type group, centered vertically on the assigned P[S] for that soil type group.

Figure 11-4 compares the SMT's P[S] assignments based on soil description with the  $I_c$ -based P[S] relationship from the CPT-based models in the Task 7 report (Section 6.1). The  $I_c$  associated with each soil type group was selected using judgment based on soil descriptions for  $I_c$  ranges by Robertson and Cabal (2015), shown in the figure with shaded vertical bands. The width of these bands reflects the relatively modest correlation between PI and  $I_c$  (e.g., Section 5.4.2.3 of the Task 7 report; Hudson et al., 2023b). The SMT's combined PI-based P[S] assignments for each soil type group (red symbols) are reasonably close to the SMT's  $I_c$ -based P[S] relationship, which gives confidence that estimates of P[S] from the SMT's CPT- or SPT-based relationships are similar. One exception is the P[S] for soils described as "silty sand", which has a significantly lower P[S] compared to the CPT-based estimate of P[S] for a soil with  $I_c$  = 2.0. This is likely due to the large standard deviation of PI for this soil type (Figure 10-5 in Section 10.3.1.2).

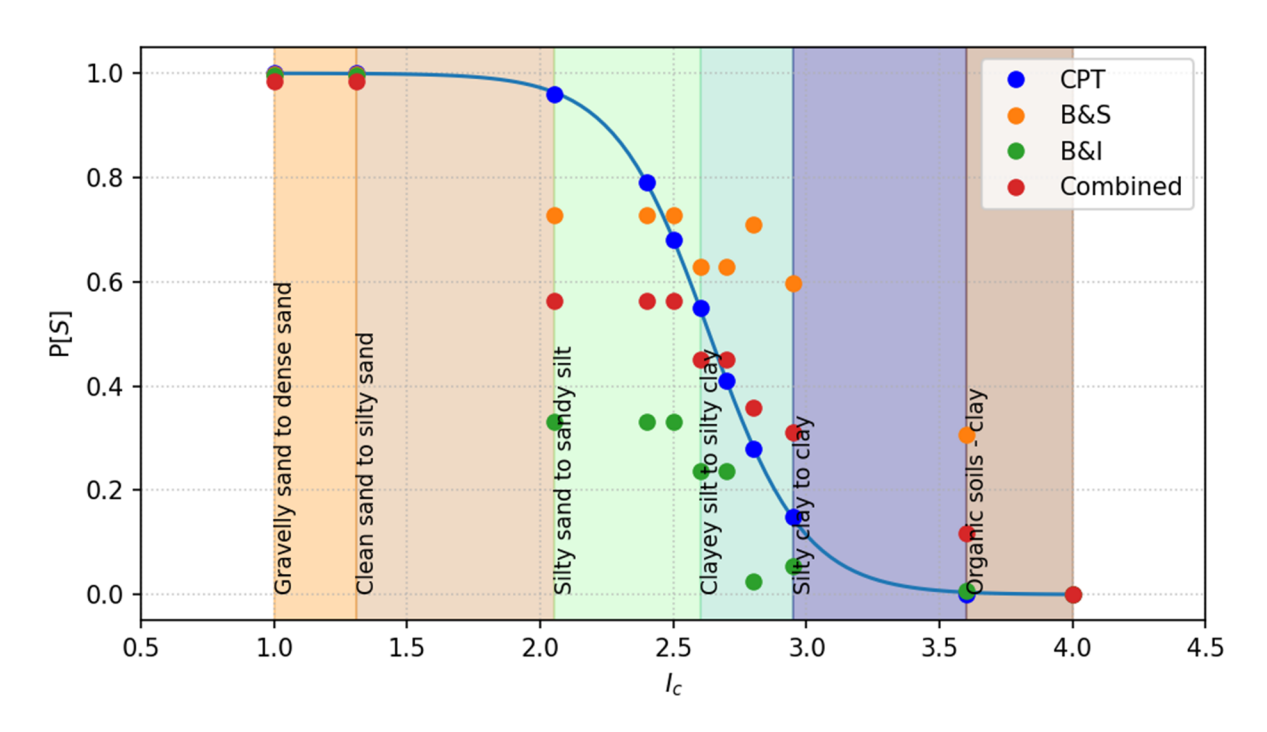


Figure 11-4 Comparison of the SMT's  $I_c$ -based P[S] model (blue line and circles) with the P[S] models based on Bray and Sancio (2006), Boulanger and Idriss (2006), and the SMT's combined model. Estimates of  $I_c$  for each soil type group are approximated based on descriptions from Robertson and Cabal (2015).

# 11.2 Probability of Triggering, P[7|S]

As described in Chapter 4 of the Task 7 report, the SMT's approach for developing coupled probabilistic models for triggering and manifestation requires a "prior" model for the probability of triggering, which would then be potentially modified from interpretation of case history data. In Section 6.2 of the Task 7 report, we developed a prior model for P[T|S] using CRR from cyclic tests performed on soil specimens in the laboratory. This model was developed based on Box-Cox transformed  $D_r$  and then adjusted to allow computation of P[T|S] as a function of CPT data. For the SPT-based models, we adopt the same prior  $D_r$ -based P[T|S] model and adjust it to allow computation of P[T|S] as a function of SPT data (i.e.,  $N_{1,60cs}$ ), as described in this section.

The D<sub>C</sub> based linear model as documented in Section 6.2.6 of the Task 7 report is:

$$\widehat{CRR} = \zeta_0 + \zeta_1 * \widehat{D_R} + \varepsilon * \sigma_{\zeta}$$
(11-5)

where  $\zeta_0$ ,  $\zeta_1$ , and  $\sigma_\zeta$  are model coefficients defined in Table 6-2 of the Task 7 report and  $\varepsilon$  is the standard normal variate (zero mean and unit standard deviation). Alternatively, the equation can be rewritten in the untransformed space as:

$$CRR = \left(\frac{D_r^{\lambda_{Dr}} \lambda_{CRR} \zeta_1}{\lambda_{Dr}} + \lambda_{CRR} \sigma_{\zeta} \varepsilon + \lambda_{CRR} \zeta_0 - \frac{\lambda_{CRR} \zeta_1}{\lambda_{Dr}} + 1\right)^{\frac{1}{\lambda_{CRR}}}$$
(11-6)

Typically, liquefaction evaluations are performed based on in situ test measurements (e.g., SPT or CPT), and  $D_r$  is not known. However,  $D_r$  can be approximated from SPT or CPT data using published correlations. In the Task 7 report, the SMT adopted a correlation recommended by Idriss and Boulanger (2008) to convert  $D_r$  to  $q_{c1Ncs}$  (Eq. 6-26). Idriss and Boulanger (2008) also recommended a correlation to convert  $D_r$  to  $N_{1,60cs}$ , which the SMT chose to adopt for our SPT-based triggering model:

$$D_r(\%) = 100 \sqrt{\frac{N_{1,60cs}}{C_d}} \tag{11-7}$$

where Idriss and Boulanger (2008) recommended  $C_d$  =46 for clean sands. Using a subset of our "intact" specimen dataset of laboratory tests (see Section 6.2.1 of the Task 7 report) where both  $D_r$  and  $N_1$  or  $N_{1,60}$  are known and chamber test data obtained from Marcuson and Bieganousky (1977), we compared the correlation between  $D_r$  and  $N_{1,60cs}$  with measured values of  $D_r$  and  $N_{1,60}$  (Figure 11-5). In cases where only  $N_1$  was known, the energy was assumed to be 80% for intact specimens and 60% for chamber tests to normalize  $N_1$  to  $N_{1,60}$ . Using  $C_d$  = 46 (solid black line) reasonably represents our data, while other recommended  $C_d$  values [e.g., 35 for depositionally "new" soils and 60 for natural soils with depositional age older than 100 years per Skempton (1986); 26 for silty sands and 51 for clean sands per Cubrinovski and Ishihara 1999] also fit within the range of the measured data. The SMT decided to adopt  $C_d$  =46.

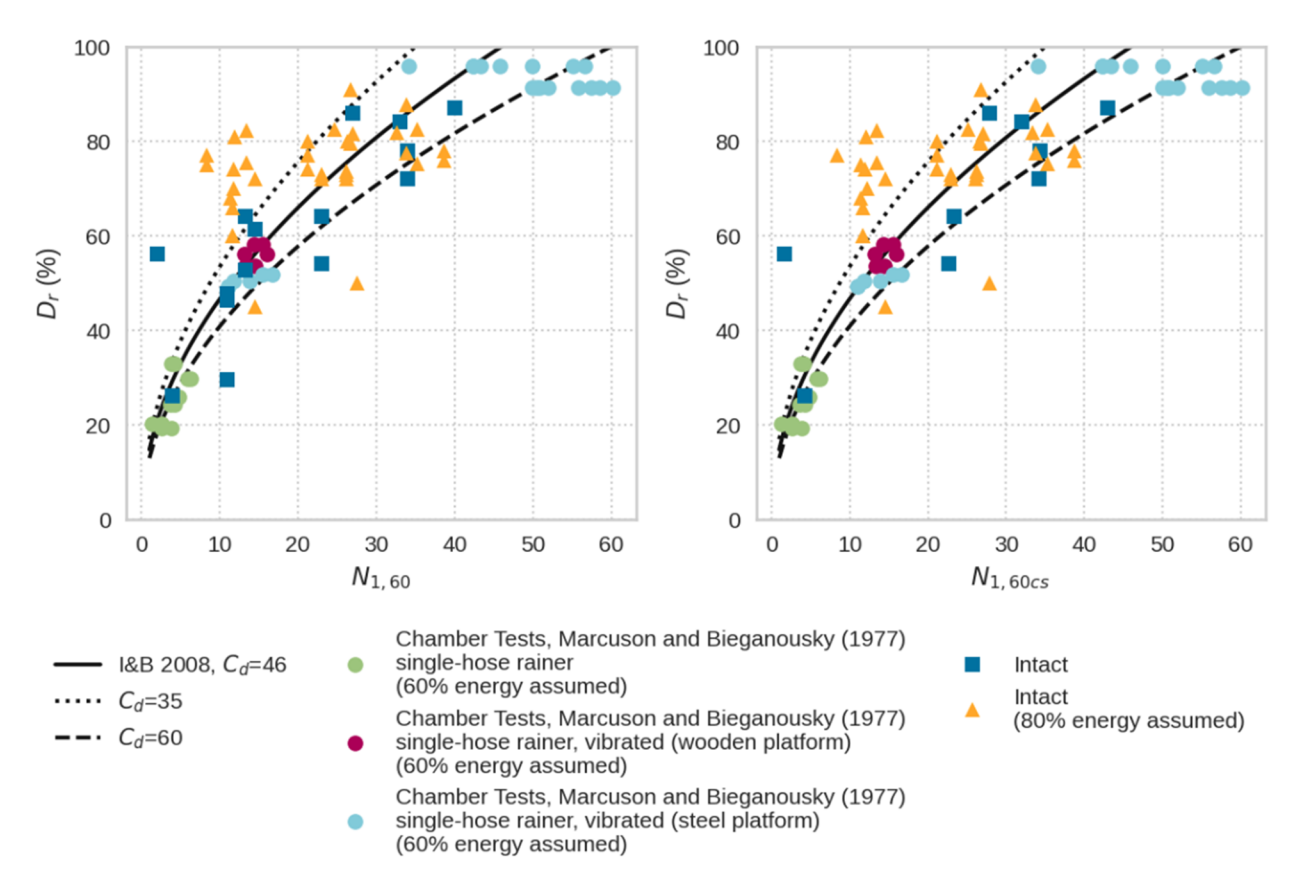


Figure 11-5 Comparison of the Idriss and Boulanger (2008) correlation between  $D_r$  and a)  $N_{1,60}$  and b)  $N_{1,60cs}$  for three fitting coefficients:  $C_d = 35$ , 46, and 60. The SMT adopted the relationship with  $C_d = 46$ .

As discussed in Section 6.2, we acknowledge that there are effects due to sample disturbance and soil fabric that cause *CRR* to be different in the laboratory compared to what is expected in the field (e.g., Seed, 1979). Our philosophy is to use results from laboratory testing to reflect the effect of state in this *CRR* relationship. This prior relationship (Eq. 11-6) is then tested against case histories through the Bayesian updating process as we develop a manifestation model (e.g., as was done for CPT-based models in Sections 6.3.2, 6.3.3, and 6.3.4). In this section, we develop the prior to be used in the Bayesian updating framework using SPT data described in Section 11.4 (and aligned with the CPT-based framework in Sections 4.4.2 and 4.4.3).

As discussed in Section 6.3.7 of the Task 7 report, we anticipate that applications of the P[T|S] models developed in this report will be of two types: (1) applications for which the desired end product is a prediction of manifestation and (2) applications for which only P[T] is of interest (i.e., the manifestation components of the model will not be used). For the first application type, the goal is to test the laboratory-based prior triggering relationship against case histories through the Bayesian updating process as we develop a manifestation model, as was done for CPT data in Section 6.3.5 and for SPT data in Section 11.5. For the second application type, following the logic developed in Section 6.3.7, the recommended central branch P[T|S] model when P[T] of a single layer is desired (i.e., triggering analysis only) using SPT data is the same as the CPT-based models: compute P[T] as the product of  $PF_{T|S}$  and  $PF_S$ , where  $PF_{T|S}$  is defined in Eq. (11-5) and uses the laboratory-based coefficients in Table 6-2. The equations to compute

P[7] using SPT data are summarized below, with equation numbers from the Task 7 report included in parentheses when the same equation is used in both the CPT- and SPT-based model.

$$P[T] = PF_{T|S}PF_{S} (11-8) (6-21)$$

where

$$PF_{T|S} = \frac{1}{1 + \exp\left(\frac{-1.702 \cdot (\widehat{CSR} - \widehat{CRR})}{0.994}\right)}$$
(11-9)  
(6-22)

$$\widehat{CSR} = \frac{\left(CSR_{M7.5,1atm}^{-0.6566} - 1\right)}{-0.6566} \tag{11-10}$$
(6-23)

$$\widehat{CRR} = -7.43 + 0.0325 \cdot \widehat{D_r} \tag{11-11}$$
(6-24)

$$\widehat{D_r} = \frac{(D_r^{1.2022} - 1)}{1.2022} \quad (D_r \text{ in \%})$$
(11-12)
(6-25)

$$PF_S = 1 - \frac{1}{1 + \exp\left(\frac{-1.702 \cdot (PI - 10.34)}{4.651}\right)}$$
(11-13)

Using these recommended equations yields CRR and  $PF_{T|S}$  values as shown in Figure 11-6 as functions of  $D_r$ , and Figure 11-7 as functions of  $N_{1,60cs}$ . Note that for  $N_{1,60cs}$  values greater than about 46, the associated  $D_r$  using the correlation in Eq. (11-7) is greater than 100%. Although a  $D_r$  greater than 100% is not theoretically correct, we acknowledge that there is inherent uncertainty in the  $D_r$ - $N_{1,60cs}$  correlation that prevents a perfect mapping between all possible values of  $N_{1,60cs}$  and corresponding values of  $D_r$ . In fact, it is common to reach blow counts equal to or greater than 50 in very dense or gravelly soils. Thus, to allow estimates of P[T|S] for soils with  $N_{1,60cs}$  greater than 46, we extend these relationships beyond the limits of the  $D_r$  to  $N_{1,60cs}$  correlation. This is depicted in Figure 11-7 as dotted lines.

Those who apply the recommended P[T|S] Eqs. (11-8) through (11-13) above for soils with  $N_{1,60cs}$  greater than 46 should carefully consider the potential causes of these high blow counts and the resulting P[T|S]. For example, it is common practice to continue an SPT until achieving "refusal", which is often considered to be 50 blows in less than the standard 0.30m penetration distance of the test. If refusal in one soil layer is achieved in 0.10m whereas refusal in another soil layer is achieved in 0.30m, both soils would be assigned the same CRR and P[T|S] if  $N_{1,60cs}$  is recorded as 50 in both cases. This is problematic because the soil that reached refusal in 0.1m could be significantly denser, older, and/or more cemented than the soil that reached refusal in 0.3m, and therefore would be expected to have a higher CRR and a lower P[T|S]. This nuance is discussed in more detail in Section 12.1.

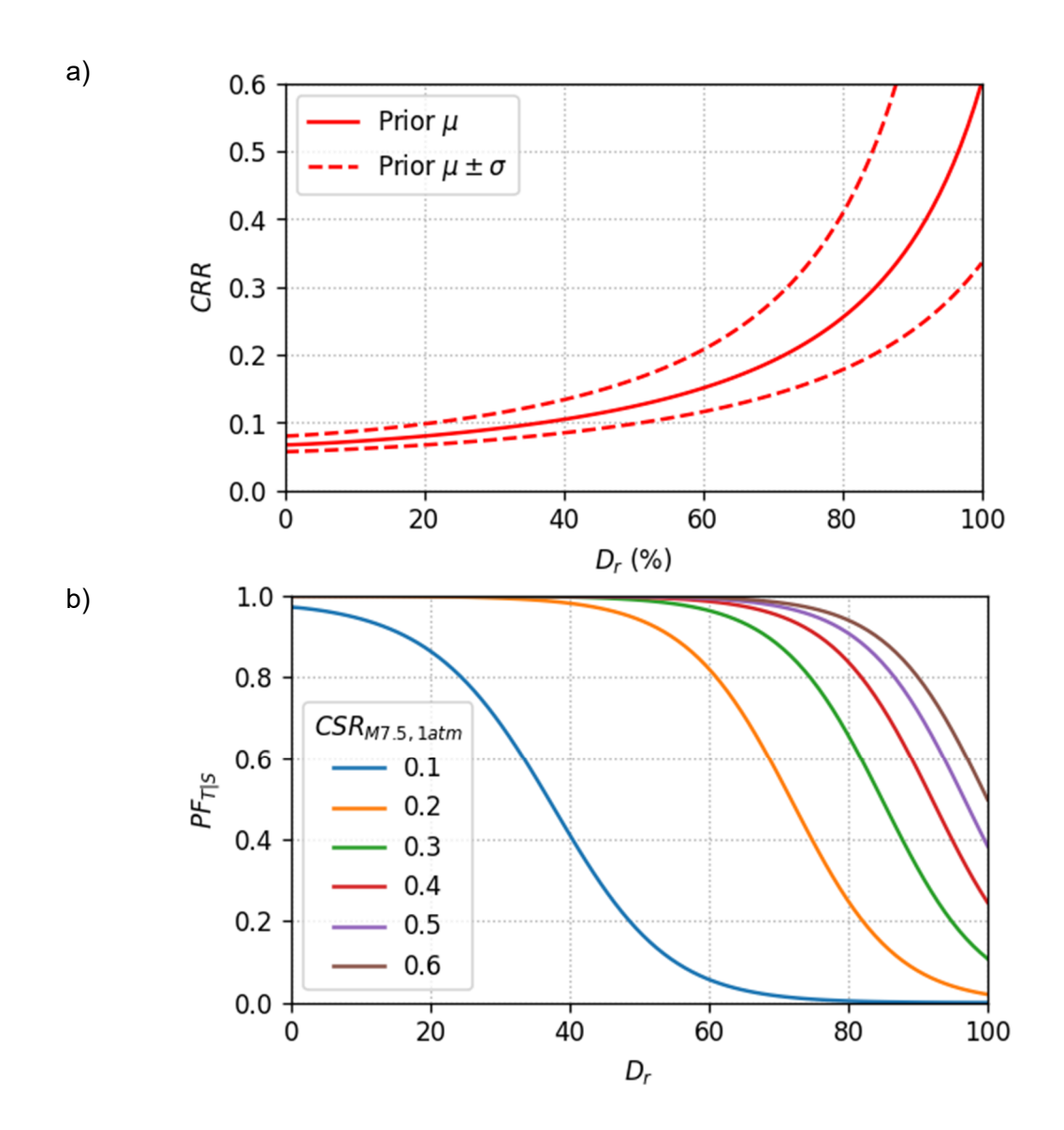


Figure 11-6 Plots of  $D_r$ -dependence of (a) CRR and (b)  $PF_{T|S}$ .

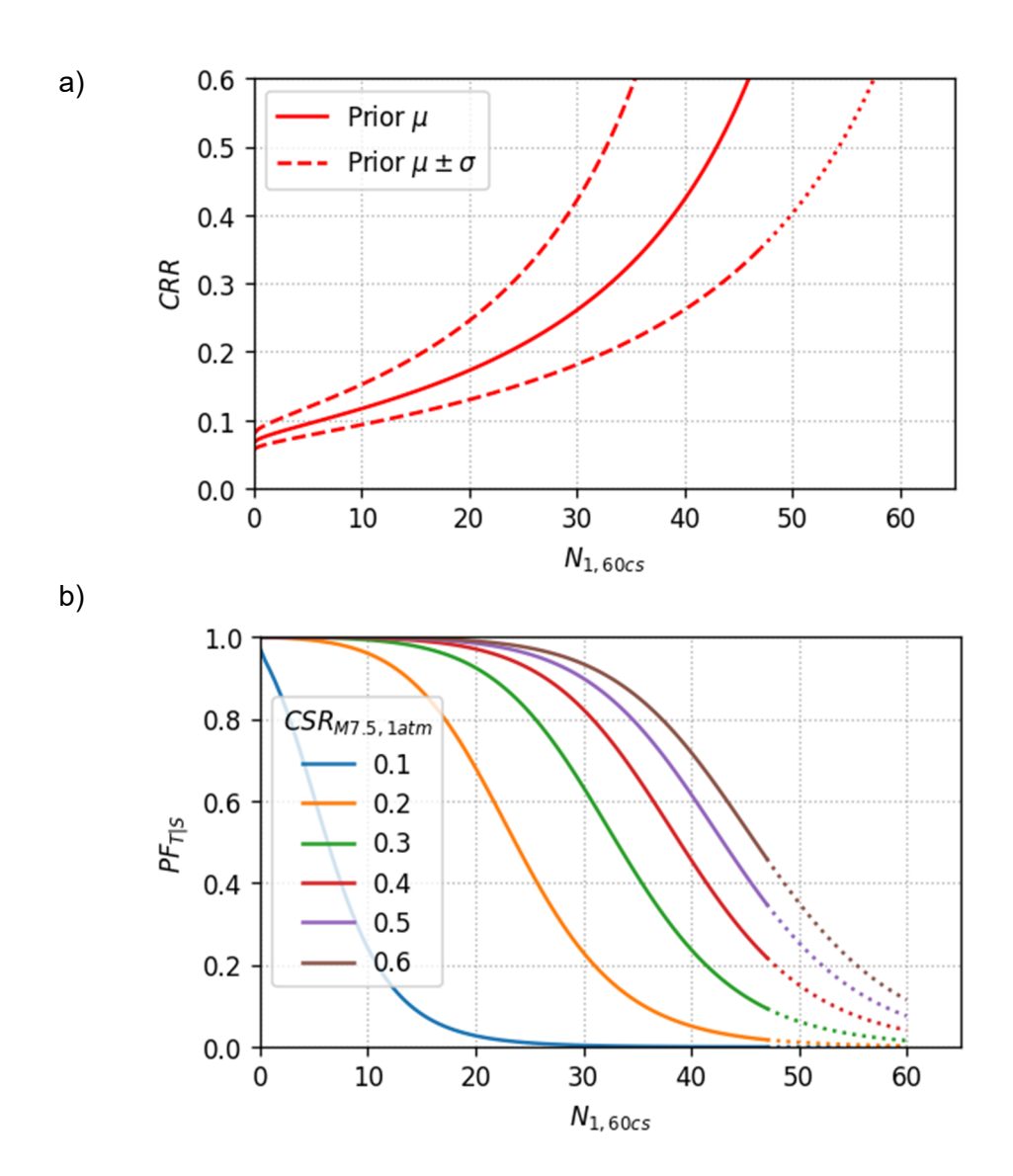


Figure 11-7 Plots of  $N_{1,60cs}$ -dependence of (a) *CRR* and (b)  $PF_{T|S}$ . Dotted lines indicate where  $N_{1,60cs}$  would yield a  $D_r > 100\%$  using the adopted correlation.

## 11.3 Example Comparisons of SPT and CPT Triggering Models

To illustrate the consistency of the SMT's CPT- and SPT-based triggering models, we compared results for a case history site with a CPT sounding and a boring performed in the same location. We chose a well-documented case history located in Moss Landing where liquefaction was observed after the 1989 Loma Prieta earthquake (Boulanger et al., 1995, 1997). According to Boulanger et al. (1995), considerable damage, including sand boils and severe cracking, was observed in the parking lot surrounding the Harbor Master's Office. Figure 11-8 provides a map of the area, including the locations of the CPT (UC-21) and the boring (UC-B3) selected for our example. This particular pair of geotechnical tests was selected because the soil profile was relatively well characterized with SPT measurements with few data gaps (e.g., there was at least one blow count in every STRA soil layer, and there were several FC and PI measurements in layers where fines were noted in the STRA descriptions), as shown in Figure 11-9.

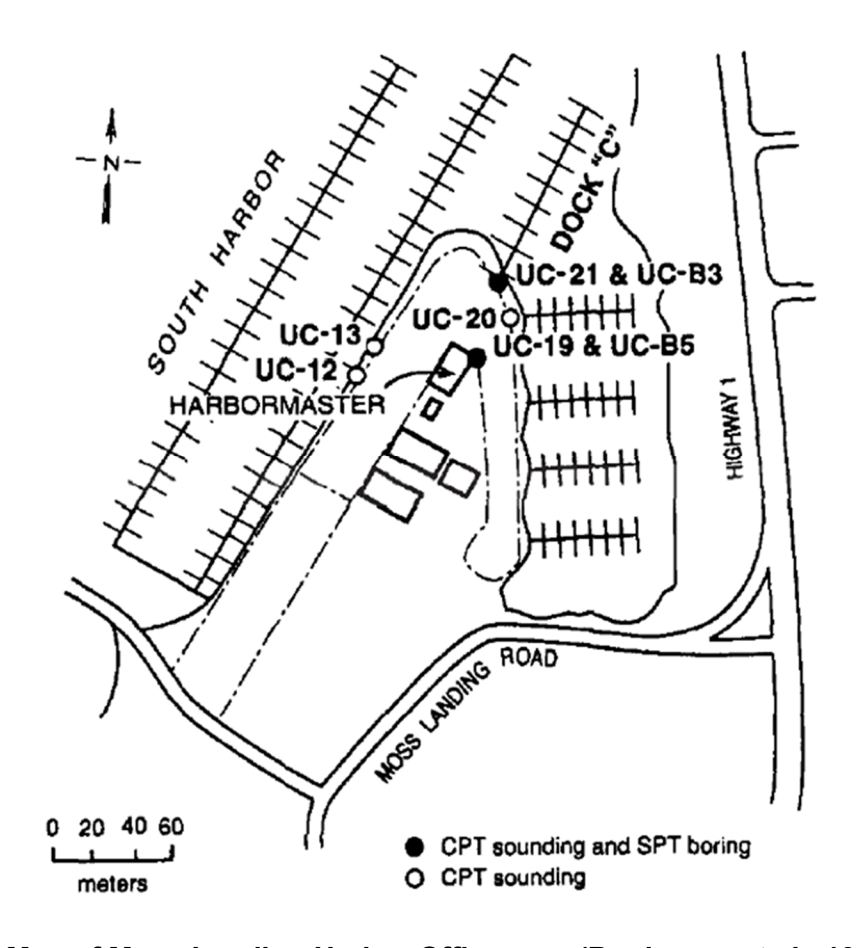


Figure 11-8 Map of Moss Landing Harbor Office area (Boulanger et al., 1995, 1997).

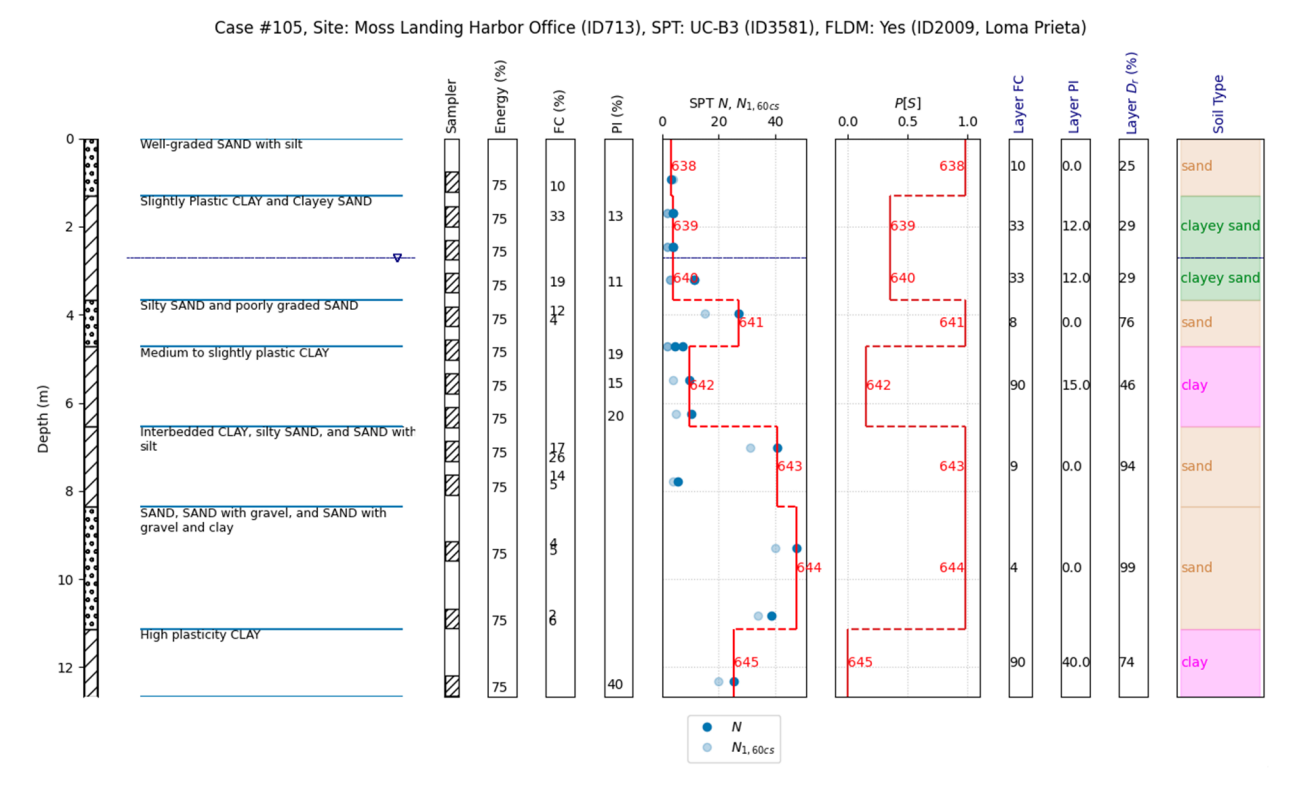


Figure 11-9 A screenshot of the SMT's Jupyter tool showing layer boundaries and representative layer characteristics for UC-B3 at Moss Landing Harbor Office.

Figure 11-10a-d shows a side-by-side comparison of the CPT data ( $q_{c1Ncs}$  and  $I_c$ ) and borehole/SPT data ( $N_{1,60cs}$  and PI) with depth, including the assigned layering based on the SMT's approaches (red lines). The figure also shows comparisons of  $CSR_{M7.5,1atm}$ , CRR, P[T|S], and P[S] for both the CPT-based models (Task 7 report) and SPT-based models (this addendum). Note that the  $K_{sat}$  parameter is not shown here but would be 0 above the groundwater table and 1 below and would be multiplied by P[T|S] and P[S] to obtain P[T].

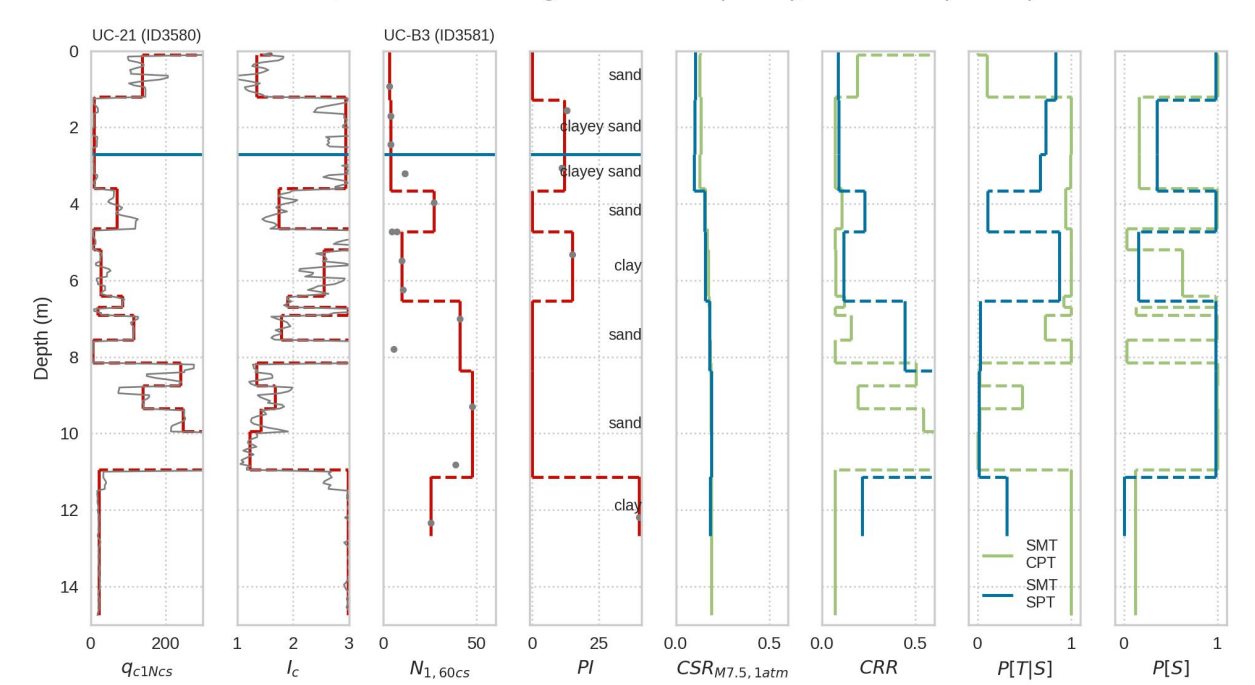
The values of  $CSR_{M7.5,1atm}$  are essentially identical between the SMT's CPT- and SPT-based models, since the equations used to compute this parameter are the same. Minor differences are due to differences in FC (which affects the  $K_{\sigma}$  calculation) and slight differences in overburden stresses due to alternative layer boundaries. The same depth to groundwater was used in both CPT and SPT profiles.

Estimates of *CRR* are generally consistent between the SMT's SPT- and CPT-models, although significant differences occur at several depth intervals:

- 3.5-4.5 m: The SPT value correlates to a higher relative density than the CPT, despite both being sand layers; this difference increases CRR for the SPT relative to that obtained for the CPT.
- 6.5-11 m: Due to more continuous data sampling enabled by using the CPT sounding, the CPT layering is more finely discretized between 6.5m and 8.3m depth where the

boring log indicates there are interbedded layers of clay, silty sand, and sand with silt. If the STRA boundaries are used, these interbedded layers are treated as one layer with a single set of representative FC, PI, and  $N_{1,60cs}$  values, which does not capture the same level of variability that the CPT layering indicates. For example, the CPT data indicates that a clay layer is present between 7.5 and 8m that is missed by the STRA layer. In addition, between 8.3 and 11m, the STRA description indicates the presence of gravels within the sand layer but does not specify the depths. More refined layer boundaries for the SPT data could address some of these discrepancies.

• > 11 m: Higher CRR values are obtained for the SPT method, but this has no practical significance because this interval is clayey and has very low P[S] from both models.



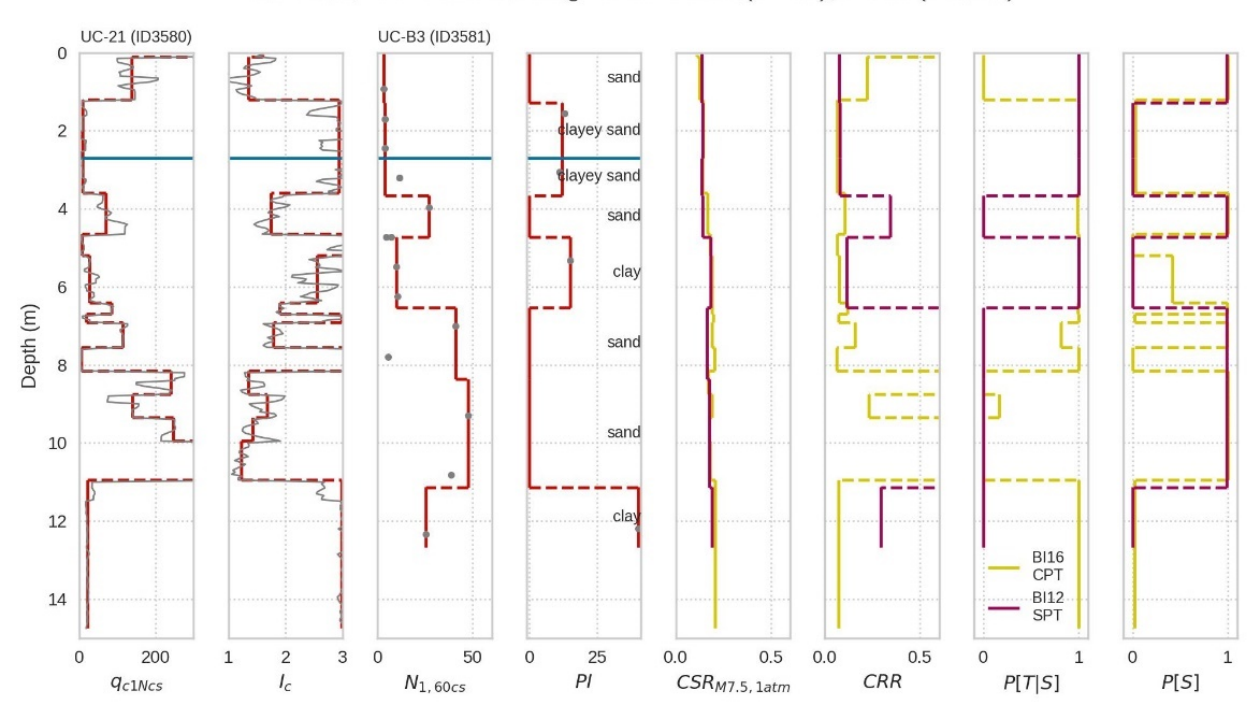
Case 105, Site: Moss Landing Harbor Office (ID713), FLDM: Yes (ID2009)

Figure 11-10 Comparison of the SMT's SPT- and CPT-based models using CPT data (UC-21) and SPT data (UC-B3) at Moss Landing Harbor Office. (a)  $q_{c1Ncs}$ , (b)  $I_c$ , (c)  $N_{160cs}$ , (d)  $CSR_{M7.5,1atm}$ , I CRR, (f) P[T|S], and (g) P[S].

Moreover, although the CPT sounding and SPT boring are marked as being in the same location in Figure 11-8, practically speaking, there was at least some separation distance between the two geotechnical explorations. This introduces some spatial variability with the potential for (i) layer boundaries of a soil layer that is present in both explorations to be offset and/or (ii) natural variability in penetration resistance, e.g.,  $q_{c1Ncs}$  or  $N_{1,60cs}$ .

The general trends in P[S] are similar for the SMT's CPT- and SPT-based models (e.g., layers that have P[S] above 0.5 using one method also tend to have P[S] above 0.5 using the other method, except for some of the interbedded layers, as discussed previously). The same can be said for P[T]S] values between the two methods.

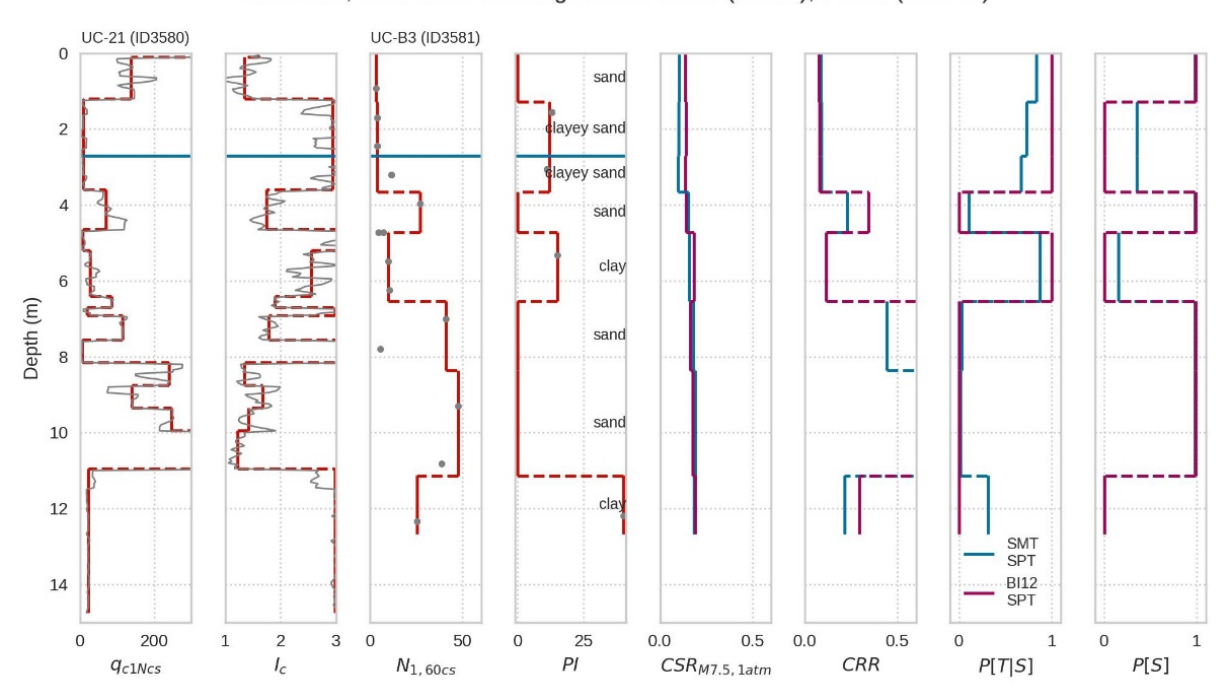
These inherent differences between the SPT- and CPT-methods using two co-located geotechnical explorations is not unique to the SMT's triggering models. These differences are also apparent when using legacy models, such as the Boulanger and Idriss (2016) CPT-based model and the Boulanger and Idriss (2012) SPT-based model, abbreviated as BI16 and BI12, respectively. This is illustrated in Figure 11-11 using the same pair of co-located explorations. The layer boundaries and representative layer characteristics (e.g.,  $N_{1,60cs}$ ,  $q_{c1Ncs}$ , FC, and PI) are sensitivee to natural variations in penetration resistance, spatial variability between two "co-located" explorations, and differences in data sampling rate. This in turn affects P[T|S] and P[S].



Case 105, Site: Moss Landing Harbor Office (ID713), FLDM (ID2009)

Figure 11-11 Comparison of the Bl12 SPT-based models and the Bl16 CPT-based models using CPT data (UC-21) and SPT data (UC-B3) at Moss Landing Harbor Office. (a)  $q_{c1Ncs}$ , (b)  $I_c$ , (c)  $N_{160cs}$ , (d)  $CSR_{M7.5,1atm}$ , I CRR, (f) P[T|S], and (g) P[S].

Finally, Figure 11-12 compares the SMT's SPT-based models with the Boulanger and Idriss (2012) SPT-based triggering model and the Boulanger and Idriss (2006) susceptibility model (as characterized by the SMT's logistic function described in Section 11.1.1). For the application of the legacy models, we interpret the layer boundaries and representative properties in the same way, so that the only differences in model outputs are from the models themselves. The SMT's  $CSR_{M7.5,1atm}$  are relatively similar to the BI12 values in this particular case, and the differences are explained by differences in the  $r_d$ ,  $K_\sigma$ , and MSF correction factors applied in each method. Note, the same PGA from the NGL database was used in both cases to compute  $CSR_{M7.5,1atm}$ , despite Boulanger et. al (1997) citing a different PGA in their original interpretation of this case history. The CRR, P[T|S] and P[S] values are functionally similar, i.e., both SMT and BI12



Case 105, Site: Moss Landing Harbor Office (ID713), FLDM (ID2009)

Figure 11-12 Comparison of the Bl12 SPT-based models and the SMT's SPT-based models using SPT data (UC-B3) at Moss Landing Harbor Office. (a)  $q_{c1Ncs}$ , (b)  $I_c$ , (c)  $N_{160cs}$ , (d)  $CSR_{M7.5,1atm}$ , (e) CRR, (f) P[T]S, and (g) P[S].

methods predict high CRR and  $P[\mathcal{T}|S]$  above 0.5 or low CRR and  $P[\mathcal{T}|S]$  below 0.5 in the same layers, and both methods predict P[S] above 0.5 or below 0.5 in the same layers. However, one notable difference is that the BI12 models tend to predict  $P[\mathcal{T}|S]$  and P[S] approximately equal to either 1.0 or 0.0 without predicting intermediate values, whereas the SMT models predict  $P[\mathcal{T}|S]$  and P[S] values that are 0.0, 1.0, and other intermediate values in between.

Additionally, it may at first appear that the SMT's lower values of P[T|S] in the shallow layers indicate that it is less conservative than BI12. However, that interpretation ignores the distinction between triggering and manifestation that is made by the SMT model. The SMT hypothesizes that the BI12 P[T|S] model depends on manifestation of some kind (e.g., sand boils or ground cracks at the surface), whereas the SMT's P[T|S] model is based on laboratory data updated by field observations and is independent of manifestation considerations. This nuance is discussed in greater detail in Section 12.2.

# 11.4 Probability of Manifestation P[M] Model Framework

As discussed in the Task 7 report (Section 4.4.3), computing  $P[M_P]$  requires specification of the prior distributions for the coefficients in the  $PF_S$ ,  $PF_{T|S}$ , and  $PF_{M|T}$  functions, and the characteristic thickness,  $t_c$ . Our approach is to develop model priors for  $PF_S$  and  $PF_{T|S}$  from laboratory data as described above, to use uninformed  $PF_{M|T}$  coefficients, and then to apply Bayesian regression to estimate posterior distributions of all coefficients. In essence, the purpose of developing a P[M] model is twofold:

- 1) To provide a model to predict manifestation of liquefaction, and
- 2) To update the coefficients assumed in the prior distributions of  $PF_S$  and  $PF_{T|S}$  based on laboratory data.

The framework to infer the coefficients for the SPT-based manifestation model using observations of manifestations at NGL sites is similar to what was presented for CPT-based models in the Task 7 report, with some modifications. This section identifies those differences.

#### 11.4.1 Manifestation Probability for a Profile

As discussed in Section 4.4.2 of the Task 7 report, the probability of manifestation of a profile  $P[M_P]$  is computed as:

$$P[M_P] = 1 - \prod_{i=1}^{N_L} (1 - PF_{M_L|T_L} PF_{T_L} K_{Sat})^{t_i/t_c}$$
(11-14)
(4-10)

where  $N_L$  is the number of layers in the profile,  $t_i$  is the thickness of the  $i^{th}$  layer, and  $t_c$  is a constant characteristic thickness. Eq. (11-14) is a simplified case that only considers contributions to manifestation from liquefaction triggering and ignores cyclic softening and non-triggering manifestations. Recall,  $PF_{M_L|T_L}$  is the *probability factor* of manifestation of a layer given triggering of the layer, defined exactly as  $P[M_L|T_L]$  in Eq. (4-8) when the thickness of the layer is equal to  $t_c$ .  $PF_{T_L}$  is the probability factor of layer triggering which is the product of the probabilistic triggering and susceptibility prior models ( $P[T|S]^*P[S]$ ).

Also recall, the expression  $P[NM_L]$  is equal to the probability that the layer will not manifest liquefaction and that  $P[NM_L] = 1 - P[M_L]$ . If none of the layer's manifest liquefaction, then the profile cannot manifest liquefaction. Therefore,  $P[NM_P]$  is computed as a product sum of  $P[NM_L]$ . However, a direct product sum (i.e., without the  $t/t_c$  term in the exponent) inherently assumes that  $P[NM_L]$  for each layer is statistically independent from all other layers. This is generally not true. The  $t/t_c$  exponent was applied to greatly reduce the influence of discretization by tying layer thickness to the characteristic length. The characteristic thickness is the layer thickness for which  $PF_{M_L|T_L}$  is statistically independent of the other layers. If all layers have a thickness equal to the characteristic thickness, then Eq. (11-14) reduces to a simple product sum. If a layer is thicker than the characteristic thickness, it becomes more likely to manifest, and vice versa. For the CPT-based manifestation model, the optimal characteristic thickness was found to be 2.0m. This characteristic layer thickness will need to be reassessed for the SPT model due to the inherent differences in SPT and CPT data (e.g., layers tend to be thicker in the SPT interpretations).

We are exploring different options for parameters to use in the SPT-based  $P[M_L|T_L]$  model. Parameters under consideration are depth to top of the layer, PI, FC, and  $N_{1,60cs}$ .

#### 11.4.2 Profile-Based Regression Framework

In Bayesian regression, prior beliefs about the model coefficients are updated using observations to form posterior beliefs about the model coefficients. The posterior distributions generally cannot be obtained in closed form, so samples are drawn from the posterior

distribution numerically using Monte Carlo methods. This regression seeks coefficients that maximize the Bernoulli log-likelihood likelihood function,

$$L = \frac{1}{N_P} \sum_{k=1}^{N_P} [y_k \ln(P[M_P]_k) + (1 - y_k) \ln(1 - P[M_P]_k)]$$
 (11-15)  
(4-12)

where  $y_k$  is a binary indicator of whether manifestation was observed at the  $k^{th}$  site ( $y_k = 1$  if manifestation was observed,  $y_k = 0$  if it was not), and  $N_P$  is the number of profiles in the database. This likelihood function is similar to those used in other probabilistic liquefaction models (e.g., Cetin et al., 2018; Moss et al., 2006).

The likelihood function exhibits several notable properties. First, if  $y_k$ =1, only the first part of the expression within the square brackets on the right side of Eq. (11-15) contributes to the likelihood function for profile k, whereas only the second expression contributes if  $y_k$ =0. Second, if the prediction is a true positive (i.e., if  $y_k$ =P[ $M_P$ ]<sub>k</sub> = 1), or a true negative (i.e., if  $y_k$ =P[ $M_P$ ]<sub>k</sub> = 0), the contribution to the likelihood function from that profile is zero. Only values of P[ $M_P$ ] that do not match the observed manifestation contribute to the likelihood function. The ideal scenario would therefore be to select an optimal set of coefficients that render P[ $M_P$ ] values that are either 0 or 1, and perfectly match the observations. In that case, the selected variables would perfectly separate the data into distinct domains, and the likelihood function would be L = 0. For real datasets, this is generally not feasible, and the value of L will therefore be less than zero.

Our approach is to adopt a NUTS algorithm (Hoffman and Gelman 2011, 2014). NUTS uses a recursive algorithm to build a set of likely candidate points that spans a wide swath of the target distribution, stopping automatically when it starts to double back and retrace its steps. The Python package PyMC (Wiecki et al., 2023) is used to perform NUTS sampling and Bayesian regression.

In the proposed framework to develop SPT-based manifestation models, in addition to the prior distributions of model coefficients, all of the training data quantities (e.g., *N*, *PI*, *FC*) are input into the regression as random variables with distributions defined using the means and standard deviations established in Section 10.3. Each of the random variables are assumed to be normally distributed with standard deviations taken as the square root of the variances described in Section 10.3 with cutoff values applied where appropriate (e.g., *PI* and *N* cannot be below 0% and *FC* cannot be below 0% or above 100%).  $N_{1,60cs}$  is computed within the random variable framework to incorporate the individual uncertainties from *N* and *FC* in the clean sand correction. This allows the quantified uncertainty for every layer's representative properties to be incorporated into the Bayesian inference and influence the posterior distributions of the model coefficients.

As discussed in Section 4.4.2 of the Task 7 report, the model formulation includes manifestation given triggering but does not include manifestation given no triggering nor manifestation given no susceptibility. The model that only considers manifestation caused by triggering therefore involves three models that each have coefficients that can be updated: susceptibility, triggering given susceptibility, and manifestation given triggering. The formulation in Eq. (11-14) can be expanded to show the susceptibility, triggering, and manifestation models that go into the profile manifestation prediction as shown in Section 4.4.2,

$$P[M_P] = 1 - \prod_{l=1}^{N_L} \left( 1 - PF_{M|T_l} PF_{T|S_l} PF_{S_l} K_{Sat_l} \right)^{t_l/t_c}$$
(11-16)
(4-11)

# 11.5 Consistency of SPT Data with CPT P[M] Model

As of the date of this report, the SPT-based  $P[M_P]$  models could not be constrained using the SPT case histories we were able to incorporate into the model development process for reasons given later in this section. We instead focused on whether the SPT case histories we have analyzed are consistent with the CPT-based manifestation model based on  $z_{top}$ ,  $PF_{M|T}(z_{top})$  (Section 6.3.3), shown in Eq. 11-17. The benefit of this model is that it can be applied to both CPT and SPT datasets since it does not involve CPT-specific measurements.

$$PF_{M|T} = \frac{1}{1 + \exp[-(2.383 - 0.375z_{top})]}$$
(11-17)

We checked the consistency of the CPT-based manifestation model  $PF_{M|T}(\mathbf{z}_{top})$  using two datasets: 1) the dataset of reviewed case histories described in Section 10.1, which only included borings co-located with one or more CPT soundings (119 profiles), and 2) a reduced dataset of profiles in which every layer has at least one measured N value (32 profiles). Although we have identified potential strategies for estimating  $N_{1,60cs}$  without measurements of N in a given layer, such strategies add considerable uncertainty to the results.

As a result, we initially examine the second dataset (the reduced dataset of reviewed profiles with at least one measured N value within every layer). Figure 11-13 shows the input models for  $PF_S$ ,  $PF_{T|S}$ , and  $PF_{M|T}$  and a confusion matrix computed using those input models on the reduced dataset of reviewed profiles with measured N values within every layer. The input  $PF_S$  and  $PF_{T|S}$  models are the laboratory-based priors as described in Sections 11.1 and 11.2, respectively. The  $PF_{M|T}$  model is the model regressed using the CPT dataset presented in Section 6.3.3. The dataset was tested using the uncertainty of variables in layers assigned as described in Section 10.3 by treating each layers' properties as a stochastic random variable and using the maximum a posteriori estimate of  $P[M_P]$  for each profile.

For comparison, the confusion matrix and performance metrics for the  $PF_{M|T}(z_{top})$  model from Section 6.3.3 computed for the CPT dataset is shown in Figure 11-14. The true positive rates for the SPT and CPT data are similar using this model. However, the true negative rate is lower for the SPT data, indicating a higher rate of false positive predictions.

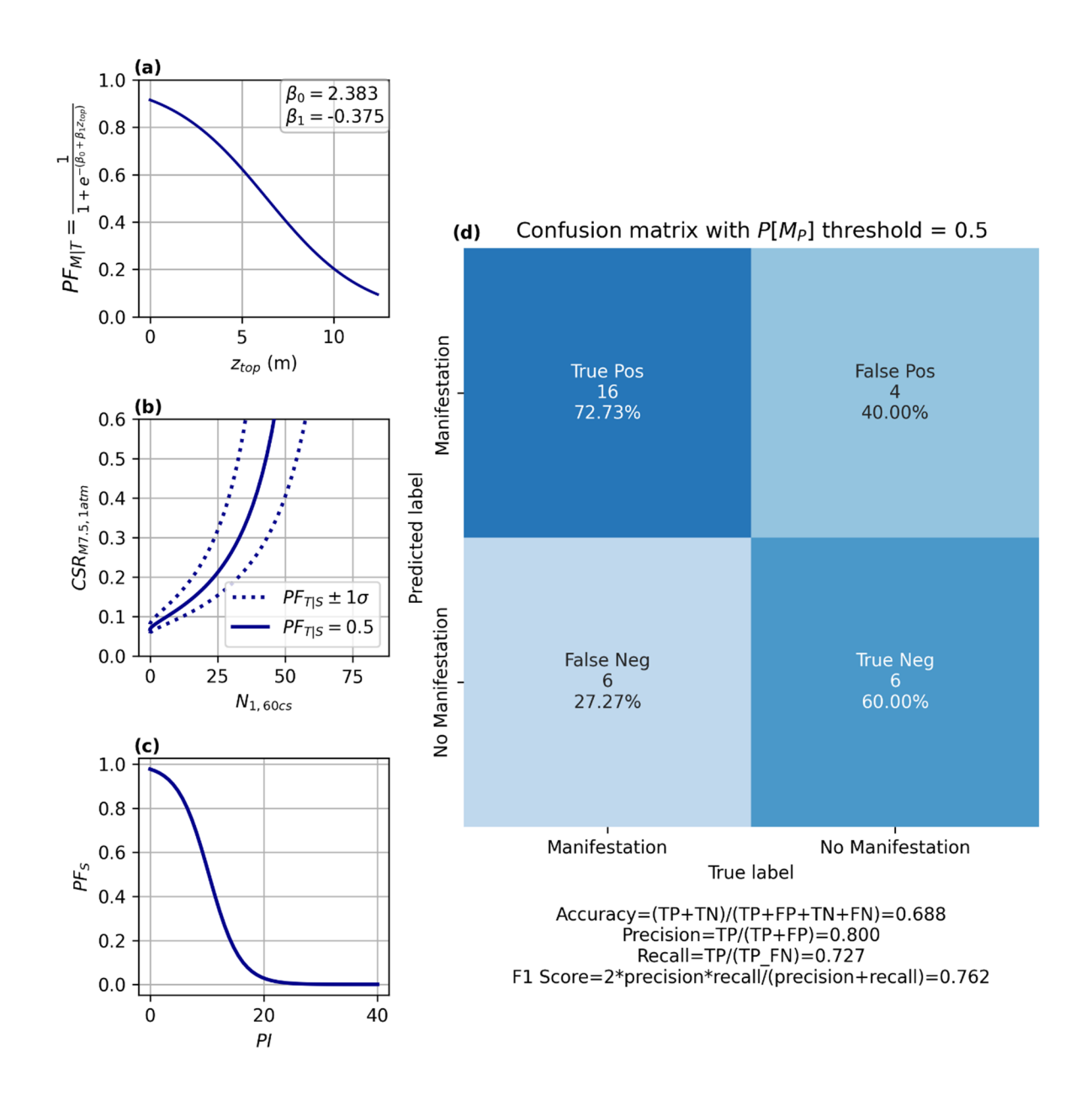


Figure 11-13 Performance of the CPT-based  $PF_{M|T}(z_{top})$  model used with the SPT dataset of reviewed profiles with a measured N value within each layer. (a), (b), and (c) present the model parameters in the relevant dataspaces for  $PF_{M|T}$ ,  $PF_{T|S}$ , and  $PF_{S}$ , respectively. (d) presents the confusion matrix and statistical metrics of the predicted  $P[M_P]$  using the model parameters in (a), (b), and (c) compared with the observation of manifestation for each of the SPT case histories in the reduced dataset.

## Confusion matrix with $P[M_P]$ threshold = 0.5

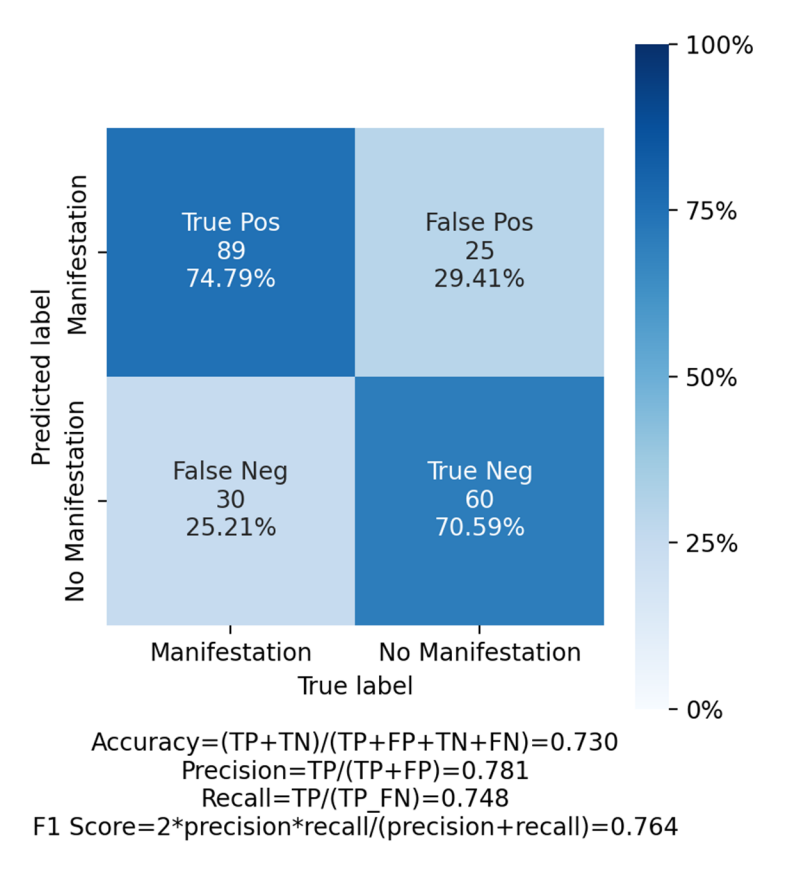


Figure 11-14 Performance of the  $PF_{M|T}(z_{top})$  model regressed using CPT data on the CPT dataset (Task 7 report).

The dataset considered in Figure 11-13 is small (32 profiles), limiting the statistical rigor of the results. To strengthen the analysis, we perform a second evaluation using the larger dataset of 119 reviewed SPT case histories. The additional cases are missing N values in some layers, which was addressed by assigning N values to layers that do not have N measurements as the nearest measured N value in the profile. For such assignments, we increase the spatial variance of N by a factor of 1.5 (Section 10.3.2). Figure 11-15 shows the results of the CPT  $PF_{M,T}(z_{top})$  model applied to the larger dataset of reviewed SPT case histories. The true positive rate increases, while the true negative rate stays approximately the same as the test on the initial (smaller) dataset, indicating slightly better performance on average for the expanded dataset.

Our interpretation of the results from these two evaluations is that the CPT  $PF_{M|T}(z_{top})$  model is reasonably consistent with the SPT dataset. In both SPT dataset test cases, the true positive rate is higher than the true negative rate, indicating a potential bias of the  $PF_{M|T}(z_{top})$  predicting manifestation over no manifestation within these test datasets.

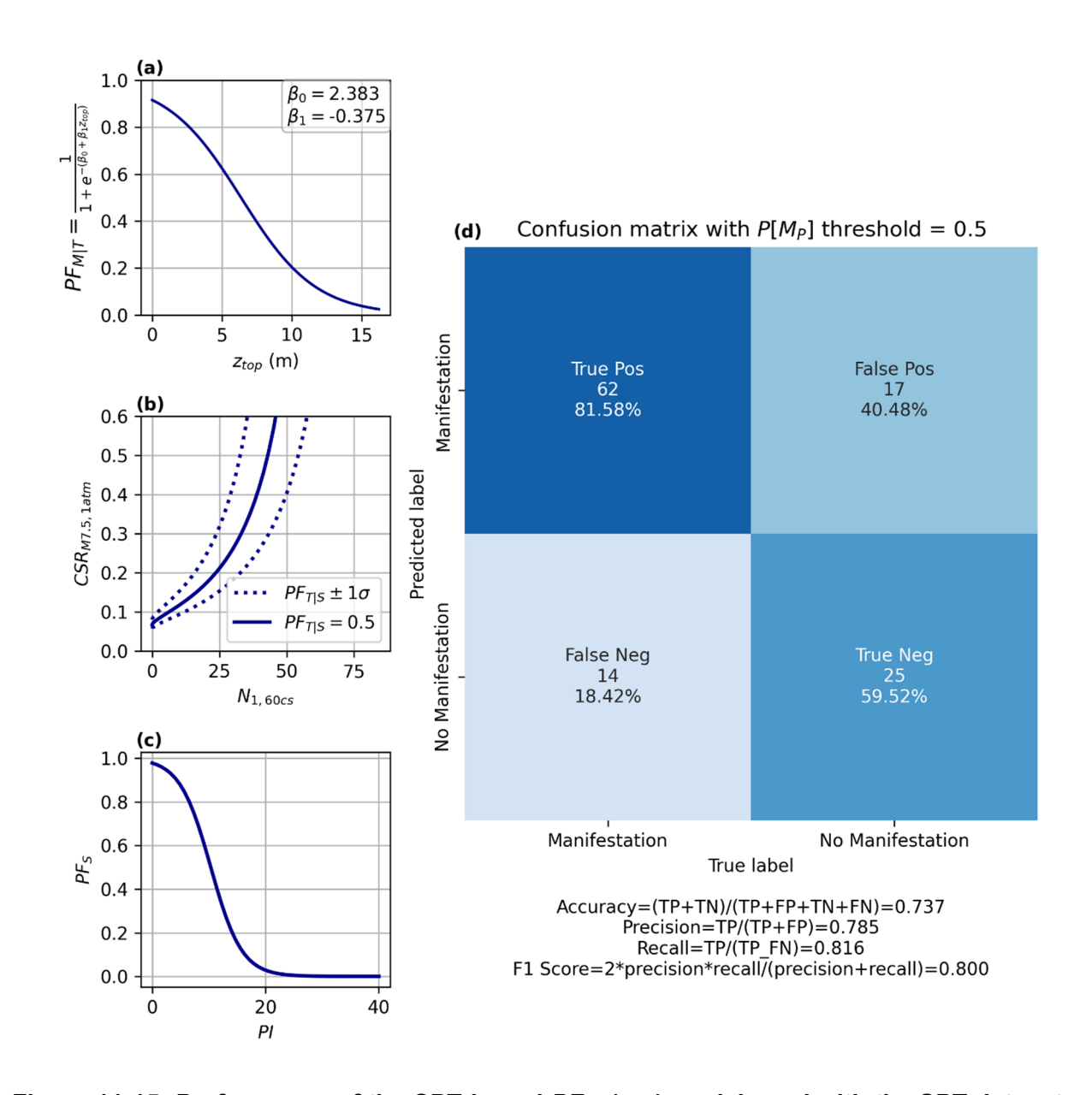


Figure 11-15 Performance of the CPT-based  $PF_{M|T}(z_{top})$  model used with the SPT dataset of all reviewed profiles. (a), (b), and (c) present the model parameters in the relevant dataspaces for  $PF_{M|T}$ ,  $PF_{T|S}$ , and  $PF_{S}$ , respectively. (d) presents the confusion matrix and statistical metrics of the predicted  $P[M_P]$  using the model parameters in (a), (b), and (c) compared with the observation of manifestation for each of the SPT case histories in the full dataset.

To provide additional insight into model performance, we apply the susceptibility and triggering model while assuming that any liquefied layer would manifest. The aim of this evaluation is to quantify the impact of the manifestation model on the results as expressed in the confusion matrix. These analyses use the larger dataset of 119 reviewed SPT case histories with a model that includes the  $PF_S$ ,  $PF_{T|S}$  priors but forces  $PF_{M|T}$  to be 1 for all layers. This model is input into the  $P[M_P]$  framework and applied to the SPT dataset, yielding the results presented in Figure 11-16. There are a high number of true positives, but a larger number of false negatives

than true negatives. This demonstrates that the application of the CPT-derived  $PF_{M|T}(z_{top})$  model improves performance. This evaluation was also performed using the Boulanger and Idriss (2012) SPT model as the  $PF_{T|S}$  model within the  $P[M_P]$  framework, and the resulting confusion matrix is presented in Figure 11-17. Using the Boulanger and Idriss (2012) model decreases the number of true positives by 11 case histories while increasing the number of true negatives by two case histories relative to the similar analysis in Figure 11-16. While the imbalance between true positives and true negatives has narrowed, overall model performance as measured by the sum of true positives and true negatives has worsened.

The above analyses confirming the applicability of the CPT-based manifestation model to subsets of SPT case histories were considered by the SMT to be the only viable approach for these analyses. Inherent shortcomings of profiles established solely based on borehole logs with SPT, including often incomplete layering and missing layer properties (penetration resistances and index tests), cause such data to be suboptimal for characterizations of layer and profile manifestation.

To regress potential future SPT-based manifestation models would require broadening the number of sites characterized for model development to expand beyond those with co-located borings and CPTs to include those with borings / SPTs only. It would also be required to develop procedures, with defined uncertainties, to overcome data gaps including missing *FC*, *PI*, or *N* in individual soil layers. These challenges and others are discussed in more detail in Section 12.1.

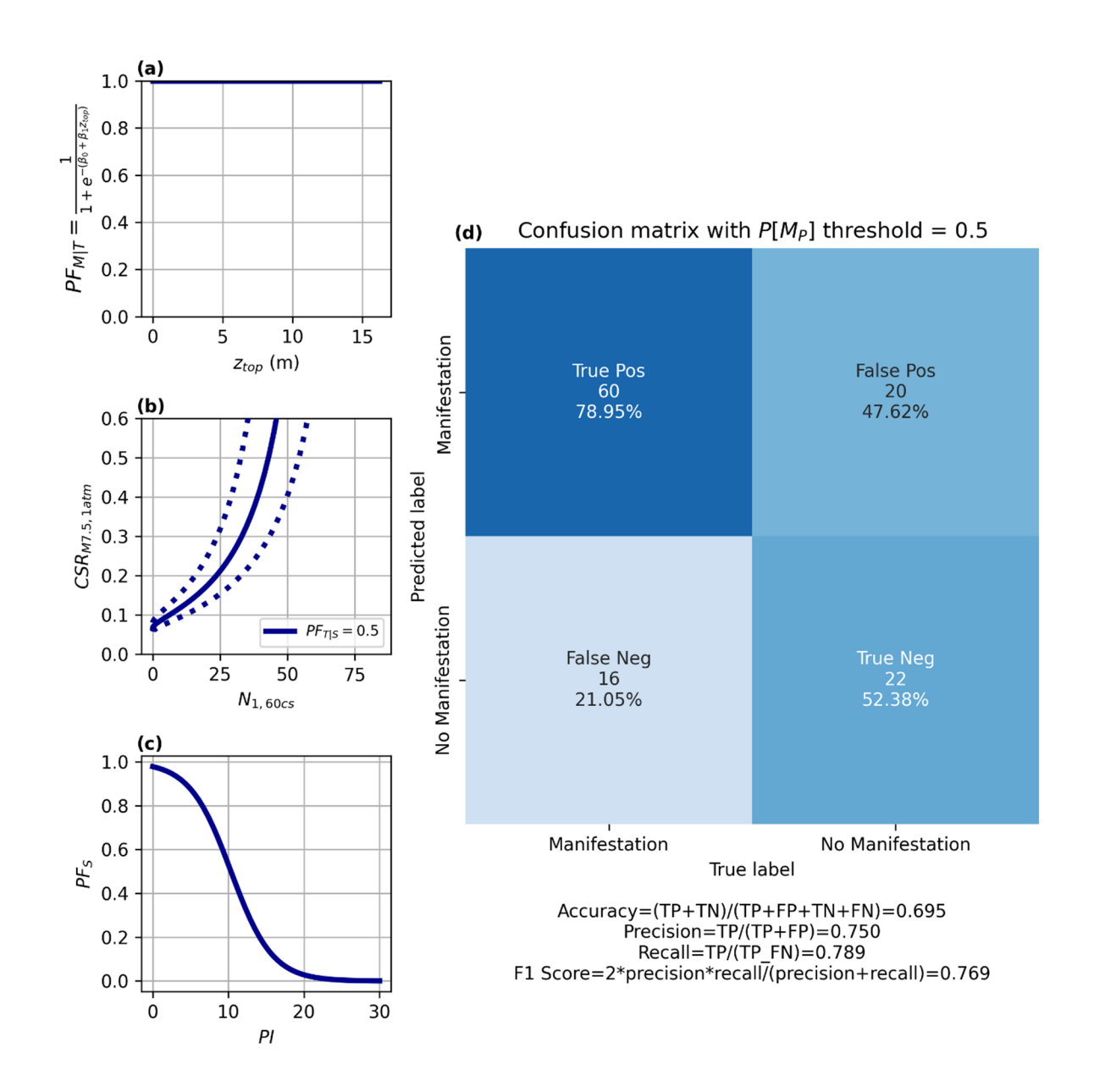


Figure 11-16 Performance of the  $P[M_P]$  model where  $PF_{M|T}$  is set to 1 for all layers in the SPT dataset of all reviewed profiles. (a), (b), and (c) present the model parameters in the relevant dataspaces for  $PF_{M|T}$ ,  $PF_{T|S}$ , and  $PF_{S}$ , respectively. (d) presents the confusion matrix and statistical metrics of the predicted  $P[M_P]$  using the model parameters in (a), (b), and (c) compared with the observation of manifestation for each of the SPT case histories in the full dataset.

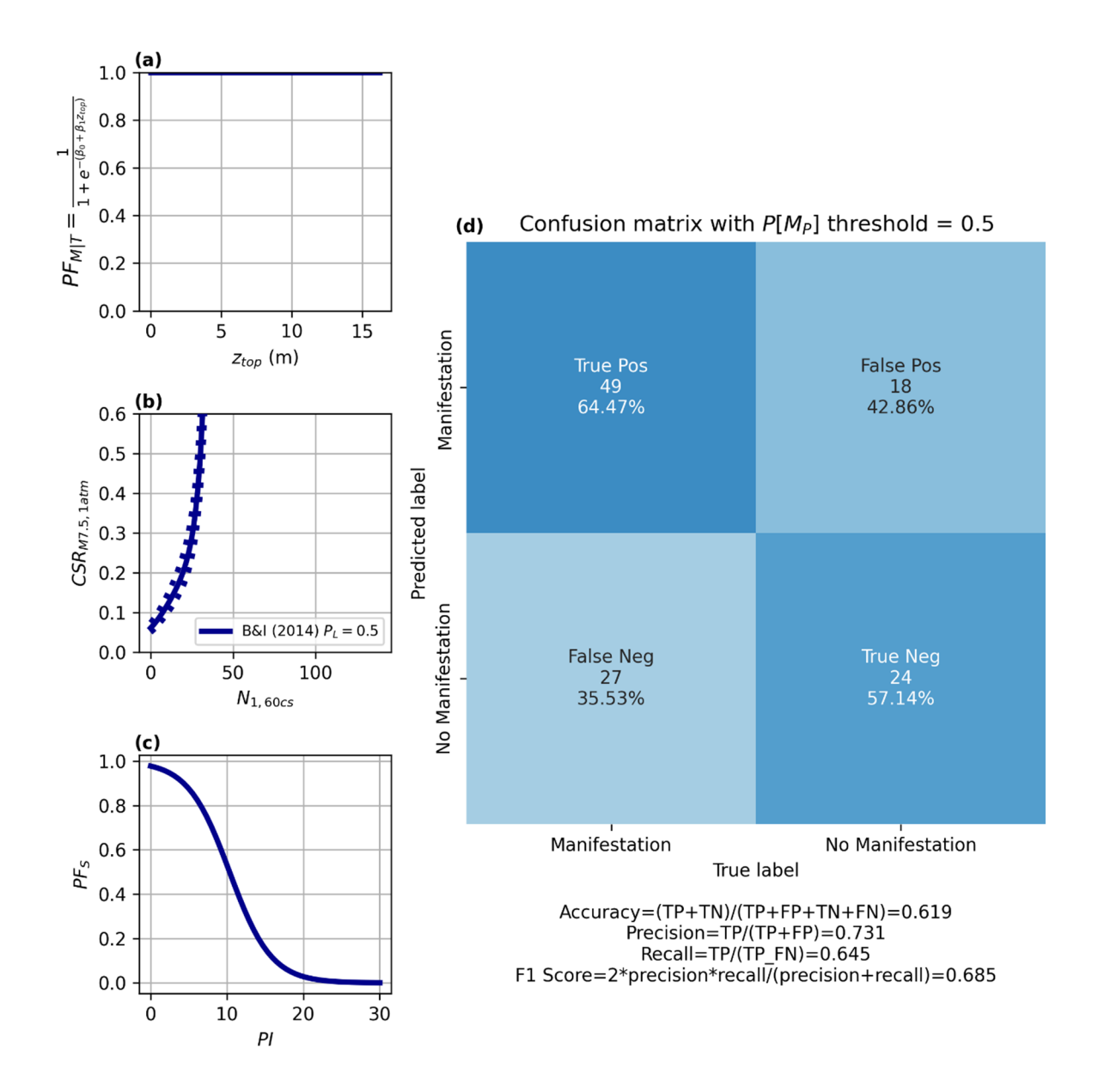


Figure 11-17 Performance of the  $P[M_P]$  model where  $PF_{M|T}$  is set to 1 for all layers in the SPT dataset of all reviewed profiles and  $PF_{T|S}$  is set to the Boulanger and Idriss (2012) model. (a), (b), and (c) present the model parameters in the relevant dataspaces for  $PF_{M|T}$ ,  $PF_{T|S}$ , and  $PF_S$ , respectively. (d) presents the confusion matrix and statistical metrics of the predicted  $P[M_P]$  using the model parameters in (a), (b), and (c) compared with the observation of manifestation for each of the SPT case histories in the full dataset.

## 12 DISCUSSION OF BOREHOLE AND SPT-BASED MODELS

In this addendum, we present probabilistic models developed by the SMT for the prediction of liquefaction susceptibility and triggering based on SPT data and present a framework for developing probabilistic models for the prediction of manifestation based on SPT data. As presented in the companion Task 7 report, we used specific definitions for those terms and formulated the models in a manner that is consistent with those definitions. For a given application, particular elements of the three-part modeling framework may be most critical. The clear separation of the components allows such determinations to be made, which in turn provides the opportunity to refine such elements through additional testing or data collection to reduce uncertainties for critical applications.

As discussed in Section 2.2 of the Task 7 report, two important philosophies influenced how this work was performed. First, we use data from the NGL database, and as such the information we relied upon is available to any interested researcher. This promotes transparency and repeatability. Second, while we exercised our experience and judgment throughout the learning and model-building process, we translated that judgment into procedures that can be consistently applied across case histories. This too promotes transparency and repeatability, while also reducing the influence of confirmation bias and allowing the models to be used in forward applications in a manner that is consistent with how they were developed.

Our modeling process has Bayesian elements, as described in Sections 4.1 and 4.2 of the Task 7 report. The main objective of the modeling process is prediction of a particular effect of liquefaction, namely surface manifestation. Within the Bayesian process that leads to such predictions, several critical model elements must be formulated, which include probability of susceptibility P[S], probability of triggering given the soil is susceptible P[T]S], probability of profile manifestation when one or more layers within the profile trigger P[ $M_P$ ] (which is conditioned on a series of variables that are not shown here for brevity). This addendum presents SPT-based models for two of these elements – P[S] (Section 11.1) and P[T]S] (Section 11.2) and provides a framework for obtaining a third element – P[ $M_P$ ] (Section 11.4).

All of the models provided in this report have empirical elements. As such, they are valid only over certain parametric ranges. The P[T|S] model mainly applies for Holocene sediments and artificial fills that are relatively granular in composition. The  $D_r$  range for the model is considered to be 20% to 90% based on the availability of laboratory data but has been extended to apply outside this range when using  $N_{160cs}$  as the input parameter (discussed in Section 11.2). The  $P[M_P]$  model is intended to predict manifestation from liquefaction at essentially level ground sites; as such it does not apply for problems involving cyclic mobility, flow slides, or ground failure from non-susceptible soils (i.e., stability problems involving strength loss in clay).

The following sections highlight important discussion topics for understanding and appropriately using the SPT-based models provided in this addendum and provide suggestions for future research topics that could improve these models.

## 12.1 Challenges in Interpreting Borehole Data

Interpretation of borehole data, including SPT blow counts, provides some benefits and some challenges relative to CPT-based methods. The primary benefit is that a geologist or geotechnical engineer performs visual manual classification of soils retrieved from the borehole during drilling, which provides insights into soil composition that are superior to soil behavior

type index,  $I_c$ , that is used when CPT testing is performed in the absence of sampling. Furthermore, laboratory tests are often performed on samples gathered from the boreholes, providing direct measurements of fines content and plasticity characteristics, and possibly cyclic strength, that are known to influence liquefaction susceptibility and triggering. Correlations between  $I_c$  and FC and PI are often quite poor, and measuring these quantities is superior to inferring them from  $I_c$ .

A significant drawback of developing a profile-based manifestation model using borehole data compared with CPT data is that SPT blow counts are sampled infrequently compared with CPT tip resistance, and sometimes no SPT blow counts are measured within an entire stratum. For example, an engineer may opt to forego (with good reason) SPTs within a fine-grained soil layer opting instead for tube samples for laboratory testing. In other cases, blow counts were simply not measured within layers having a non-negligible probability of susceptibility. For example, in Figure 10-2, a stratum at Moss Landing Marine Lab between approximately 9 and 13 m depth is described as "Clay and sand (CL-SP)" in the stratigraphic log. Based on the soil description, a mix of susceptible and non-susceptible soils would be expected within the stratum. However, blow counts were not measured in this layer, and assigning a probability of triggering and manifestation therefore cannot be performed on measured penetration resistance values. In a traditional liquefaction triggering assessment, the path forward is clear. The critical layer would simply be selected as the sandy layer overlying the "Clay and sand" stratum. But in a profile-based framework, every layer contributes to the overall manifestation probability.

Low plasticity fine-grained soils have a non-zero probability of susceptibility in our model, and therefore must be evaluated for liquefaction triggering. SPT-based liquefaction triggering relationships use blow counts that must be corrected for the effects of non-zero fines contents. However, fines content corrections have been formulated for sandy soils with predominantly non-plastic silts, and any bias introduced by applying these fines content corrections to plastic fine-grained soils is currently not well understood. We anticipate that fine-grained soil will generally have a higher cyclic strength than implied by inserting their fines-corrected blow count values into a CRR equation because they are likely to be undrained during penetration resistance tests. High pore pressures that persist between blow counts will reduce the measured blow count. Furthermore, bearing factors at the tip of a sampler are different for drained and undrained loading, and drained tip resistance is generally significantly higher than undrained as a result. We contend that sampling and cyclically testing these materials is the best way to assess their cyclic strength, but such testing is not available in most of the case histories in the NGL database, and for none of the ones used herein.

A number of methods could potentially be used to fill in gaps in penetration resistance measurements. First, soil layers with missing blow count data could be assumed to be non-susceptible based on the observation that an engineer or geologist would have measured blow count values in all susceptible layers. Interestingly, Saye et al. (2021) attributed observed ground failure at the Moss Landing Marine Lab to failure of a fine-grained soil layer rather than to liquefaction of the sand layer assigned as the critical layer by Boulanger and Idriss (2016). Saye et al. (2021) utilized CPT data instead of SPT data to make this inference, but the point remains that important aspects of the performance of a profile may be missed if fine-grained soil layers (which are disproportionately more likely to not have SPT blow counts) are excluded from consideration. Second, susceptibility and triggering could be based on laboratory tests performed on the fine-grained soils. Ideally, plasticity characteristics would be measured using the Atterberg limits test, and both susceptibility and cyclic strength would be evaluated using a cyclic testing program (e.g., direct simple shear or triaxial testing). Atterberg limits are often

measured for fine-grained soils. However, cyclic strength testing is rarely performed. Third, the cyclic strength of fine-grained soils could be characterized using CPT data instead of borehole information. In these cases, we argue that the cone tip resistance should also be utilized to characterize the sandy soils because CPT measurements are more repeatable than SPT measurements. Finally, the penetration resistance could be inferred from visual manual classification (e.g., qualitative soil descriptions such as hard/stiff/soft), or from measurements in similar layers within the profile. However, the resulting inferred values would be highly uncertain.

Uncertainty in SPT blow counts arise from measurement errors, and from soil spatial variability. Blow count measurements carry significant uncertainty due to (i) hammer energy being rarely measured, (ii) upward migration of water in hollow-stem auger borings when adequate pressure head is not maintained, (iii) use of non-standard sampling equipment such as the modified California sampler, or SPT samplers modified to accommodate rings, (iv) rod length corrections, and other factors. By contrast, measurement error in CPT tip resistance is due to the calibration coefficient in the cone tip load cell, and potentially push rate. For these reasons, we consider SPT blow counts to carry significant measurement uncertainty compared with CPT tip resistance. Furthermore, soils are spatially variable due to the depositional processes that formed them. Both SPT and CPT result in some depth-averaging such that the measured penetration resistance is not a point measurement, but rather an average within a zone of influence. Averaging is more significant for SPTs because the single blow count is measured for a full 0.30m of sampler penetration. Furthermore, a handful of SPT measurements might be obtained within a stratum, which does not permit a robust quantification of within-layer variability. It is therefore often unclear whether the selected SPT blow count is truly representative of the layer.

Another challenge is that SPT blow counts are often terminated in stiff soils before the sampler is advanced one foot, resulting in refusal or a blow count reported as, for example, 50/4" where 50 blows were applied to the sampler, but it only advanced 4" before the test was terminated. Using typical correlation relationships (Section 11.2), uncemented sandy soils are inferred as having a blow count around 46 when  $D_R = 100\%$ , so there is arguably no meaning to continuing SPT measurements beyond this threshold. However, soils with blow counts higher than the threshold are likely cemented, thereby increasing the blow counts in a manner that makes liquefaction assessments difficult since our procedures are formulated for uncemented sands. It is likely that refusal soils have higher liquefaction resistance than uncemented sands with  $D_R = 100\%$ . Yet assessing the cyclic strengths of these materials is not currently possible. This is the reason we have opted to extrapolate cyclic strength with blow counts in Figure 11-7.

## 12.2 Triggering and Manifestation

The reliance upon field data in the development of empirical models of liquefaction potential has been well established and widely accepted for many years. This approach was based on the difficulty of obtaining undisturbed samples of clean, liquefiable sands and the observation that different methods of specimen reconstitution produced very different levels of cyclic strength in laboratory tests (e.g., Seed 1979). As a result, in U.S. practice laboratory tests have tended to be relegated to the investigation of constitutive behavior (e.g., phase transformation, cyclic degradation) under carefully controlled conditions and to establishing trends in behavior with respect to variables (e.g., initial effective stress) that significantly influence behavior in the field. Advances in soil sampling technology, such as by ground freezing, have proven to be expensive and are not commonly used in the U.S., although they are used more commonly in Japan.

Current empirical models generally use the presence or absence of surficial features such as sand boils or ground surface cracking as evidence of the triggering or non-triggering of liquefaction in a given earthquake. These features, which are often referred to as "surface manifestation" are implicitly assumed to be perfect indicators of the triggering of liquefaction in the earthquakes that produced, or didn't produce, them. However, it is widely recognized that liquefaction can be triggered, for example in a thin or deep soil layer, without producing sand boils or ground cracking. It is also possible for ground cracking to be associated with cyclic softening of clay-like soils or, potentially, by elevated pore pressures not reaching 100% pore pressure ratio in thick, shallow sand-like soils. As such, it could be argued that the factor of safety produced by these empirical models describes the potential for surface manifestation more accurately than the potential for the actual triggering of liquefaction.

The triggering of liquefaction is characterized by a significant reduction in effective stress and consequent reduction of stiffness, which can lead to a number of different consequences that involve different elemental and soil profile behaviors. The development of sand boils, for example, involves the hydrologic characteristics of a soil profile in addition to the mechanistic behavior of the liquefiable soils within it. The development of ground cracking is influenced by the behaviors of both liquefiable and non-liquefiable soils, such as the cyclic degradation of saturated clay-like soils and the brittleness of overlying, non-liquefied "crustal" soils. Thin, loose layers that may not expel enough porewater to contribute to sand boil development, however, may develop sufficient shear strains to contribute significantly to lateral spreading or, in extreme cases, flow sliding.

Thus, the triggering of liquefaction can be viewed as a fundamental condition from which numerous consequences can emanate. The presence of sand boils and ground cracking are two such consequences but there are others that involve different mechanisms and are influenced by different profile characteristics. While conventional surface manifestation involves mechanisms similar to those that influenced post-earthquake free-field settlement, the most damaging consequences of liquefaction are generally associated with shearing mechanisms that produce significant lateral (and vertical) permanent deformations. The prediction of consequences that involve shearing deformations given triggering are likely to be more accurate, i.e., less biased and/or uncertain, than their prediction given conventional surface manifestation.

The models developed in the NGL project by the SMT have produced both triggering and manifestation relationships and plots of those relationships as functions of penetration resistance show triggering curves that fall below manifestation curves, particularly at higher penetration resistances (e.g., Figure 11-6a). The triggering curve may be interpreted by some engineers as a more "conservative" relationship because it implies that triggering would occur at a lower cyclic stress ratio than the manifestation curve. It should, however, be viewed as a more accurate indication of the actual triggering of liquefaction and the more appropriate point from which to conduct consequence analyses. The severity of most consequences will decrease with increasing soil penetration resistance so the consequences for soils whose triggering curves plot farthest below the manifestation curve may not be severe at all. They would be mild, however, because of consequence behavior, not because similar soils at other locations did not produce sand boils or ground surface cracking in other earthquakes. Given that the consequences of liquefaction are of greatest importance for design and performance assessment, the ability to predict consequences as accurately as possible is of paramount importance.

The development of probabilistic performance-based earthquake engineering procedures for soil liquefaction has centered on a conditional susceptibility-triggering-consequence sequence of assessments. In this approach, triggering is conditional upon susceptibility and consequences are conditional upon triggering. The distinction between triggering and manifestation that has been made in the NGL project allows this performance-based earthquake engineering approach to be implemented in a natural and logical manner. Without this distinction, the developers of consequence models are forced to predict consequences of one type to be based on a consequence of a different type, e.g., predicting lateral spreading displacement conditional upon sand boil observations, even though those observations are influenced by hydrologic profile characteristics different than those that influence lateral spreading. The development of improved consequence models, for a variety of liquefaction consequences, is an important research need in geotechnical earthquake engineering.

## 12.3 Future Work

As we developed the SPT-based models documented in this addendum, we have identified other improvements or enhancements that could be incorporated but that were not feasible within the scope and limitations of the current project. In addition to the suggestions already listed in Chapter 7 of the Task 7 report, the following suggestions are listed here as opportunities for future work.

- As part of the current project, it is necessary to broaden the numbers of sites characterized for model development to expand beyond those with co-located borings and CPTs to include those with borings / SPTs only.
- There are opportunities to refine the specific elements of SPT case history processing.

## For example:

- Refining the energy estimates when they are not measured and provided in the NGL database. Some assumptions based on region where the test was performed, age of the test, and perhaps descriptions of the equipment could help refine these estimates.
- Refining the assumed *N* value for a layer that does not have SPT measurements. There are several possible methods, some are listed in Section 12.1.
- In developing the proposed models, we have adopted some prior modeling conventions that are important, including:
  - fines corrections to convert  $N_{1,60}$  to  $N_{1,60cs}$  (Section 10.3.2),
  - $\circ$  conversions of  $D_r$  to  $N_{1,60cs}$  (Section 11.2), and
  - plasticity-based models for liquefaction susceptibility (Section 11.1).

As discussed in Chapter 7 of the Task 7 report, these prior modeling conventions may be improved in the future. For example, a subsequent phase of the NGL project will investigate the potential for improvement of susceptibility models (Stuedlein et al., 2023). For fines, there is a need to separate fines effects on  $N_{1,60cs}$  from its effect on triggering

and to refine the fines correction to convert  $N_{1,60}$  to  $N_{1,60cs}$  for reasons discussed in Section 12.1).

• Application of the  $P[M_P]$  framework described in Section 11.4 to develop probabilistic profile manifestation models suitable for use with SPT-based site characterization data.

# 13 CONCLUSIONS, SPT-BASED MODELS

In this addendum, we provide liquefaction models based on borehole logs and SPT resistance values that follow the same framework outlined in the Task 7 report, which focused on CPT data. The model framework includes discrete steps for susceptibility, triggering, and manifestation. The models provided in this report are for susceptibility (P[S]) and triggering conditioned on susceptibility (P[T]S), while a framework for manifestation analysis is provided.

In this addendum, we described several aspects of the model development process that are unique to the SPT-based site characterization data, such as:

- identifying case histories with SPT-based site characterization data from the extensive NGL case history database (Section 10.1),
- using algorithms to process site data and provide a repeatable, consistent, and objective view of the data (Chapter 10),
- identifying layers from the borehole data (Section 10.2),
- evaluating probabilistic distributions of relevant engineering properties (*PI*, *FC*, and *N*-values) for each layer (Section 10.3),
- developing a Bayesian prior model for susceptibility, P[S], for soil layers with measured PI values (Section 11.1.1)
- interpreting P[S] when PI data is not available using interpretations of soil properties from borehole strata text descriptions by jointly considering modeling uncertainty and parametric variability (Section 11.1.2),
- developing a Bayesian prior probability for triggering, P[T|S], using laboratory data adapted to utilize SPT data as the input parameter, e.g.,  $N_{160cs}$  (Section 11.2), and
- providing a framework to model surface manifestation,  $P[M_P]$ , as a function of SPT-based site characterization data (Section 11.4) and confirmed that the SPT case histories we have analyzed are consistent with the CPT-based manifestation model based on  $z_{top}$ .

For forward analysis using SPT data where P[T] of a single layer is desired (i.e., excluding manifestation), we recommend computing P[T] as  $PF_{T|S}$  multiplied by  $PF_S$  given by Eq. (11-8) through Eq. (11-13) in Section 11.2, where  $PF_{T|S}$  relies on laboratory data, for reasons given in the Task 7 report (Section 6.3.7) and in this addendum (Section 11.2).

Findings provided in this addendum are nearing their final form, although future refinements and improvements are possible. The content presented here is subject to change as we refine the methodologies, input parameters, and framework.

Although the SPT- and CPT-based models rely on several common elements, the SPT-based manifestation models are less mature than the CPT-based models, due in part to challenges with interpreting SPT-based case histories and inconsistent data density, as discussed in Section 12.1, and due to limitations of the project schedule. Opportunities for future work listed in Section 12.3 may address the discrepancy in model refinement and maturity.

While the general concepts behind our approach and the CPT-based models have been shared in meetings with the NGL Advisory Board, the MRT, and other NGL modeling teams, this addendum presents new relationships specifically for applications using SPT-based site characterization data. Accordingly, we look forward to receiving feedback on these specific relationships from the liquefaction research community as they mature and feedback from regulatory agencies, topical experts, practicing engineers, and others about the modeling approach and the reasonableness and practicality for application of the models that are documented in this report.

#### 14 REFERENCES

Boulanger, R.W. and I.M. Idriss. "CPT-Based Liquefaction Triggering Procedure." *Journal of Geotechnical and Geoenvironmental Engineering*. Vol. 142, No. 2. 2016.

Boulanger, R. and I.M. Idriss. "CPT and SPT Based Liquefaction Triggering Procedures." Report No. UCD/CGM-14/01. Center for Geotechnical Modeling. University of California, Davis. 2014.

Boulanger, R.W. and I.M. Idriss. "Probabilistic Standard Penetration Test-based Liquefaction-Triggering Procedure." *Journal of Geotechnical and Geoenvironmental Engineering*. Vol. 138, No. 10. pp.1,185–1,195. 2012.

Boulanger, R.W. and I.M. Idriss. "Liquefaction Susceptibility Criteria for Silts and Clays." *Journal of Geotechnical and Geoenvironmental Engineering*. Vol. 132, No. 11, pp. 1,413–1,426. 2006.

Boulanger, R.W., L.H. Mejia, and I.M. Idriss. "Liquefaction at Moss Landing During Loma Prieta Earthquake." *Journal of Geotechnical and Geoenvironmental Engineering.* Vol. 123, No. 5. pp. 453–467. 1997.

Boulanger, R.W., I.M. Idriss, and L.H. Mejia. "Investigation and Evaluation of Liquefaction Related Ground Displacements at Moss Landing During the 1989 Loma Prieta Earthquake." Report No. UCD/CGM-95/02. Center for Geotechnical Modeling, Department of Civil & Environmental Engineering, University of California Davis. 1995.

Box, G.E.P. and D.R. Cox. "An Analysis of Transformations." *Journal of the Royal Statistical Society, Series B (Statistical Methodology)*. Vol. 26, No. 2. pp. 211–252. 1964.

Bray, J.D. and R.B. Sancio. "Assessment of the Liquefaction Susceptibility of Fine-Grained Soils." *Journal of Geotechnical and Geoenvironmental Engineering*. Vol 132, No. 9. pp. 1,165–1,177. September 2006.

Burrington, R.S. and D.C. May, Jr. *Handbook of probability and statistics*. McGraw-Hill Book Company. New York, New York. 1970.

Cetin, K.O., R.B. Seed, R.E. Kayen, R.E. Moss, H.T. Bilge, M. Ilgac, and K. Chowdhury. "SPT-based Probabilistic and Deterministic Assessment of Seismic Soil Liquefaction Triggering Hazard." *Soil Dynamics and Earthquake Engineering*. Vol. 115. pp. 698–709. 2018.

Cubrinovski, M. and K. Ishihara. "Empirical Correlation Between SPT N-value and Relative Density for Sandy Soils." *Soils and Foundations.* Vol. 39, No. 5. pp. 61–71. 1999.

Hoffman, M.D. and A. Gelman. "The No-U-Turn Sampler: Adaptively Setting Path Lengths in Hamiltonian Monte Carlo." *Journal of Machine Learning Research.* Vol. 15, No. 47. pp. 1,593–1,623. 2014.

Hoffman, M.D. and A. Gelman. "The No-U-Turn Sampler: Adaptively Setting Path Lengths in Hamiltonian Monte Carlo." arXiv. <a href="https://doi.org/10.48550/ARXIV.1111.4246">https://doi.org/10.48550/ARXIV.1111.4246</a>. 2011.

Huang, Y.M. *Performance-based design and evaluation for liquefaction-related seismic hazards*. Ph.D. Dissertation. University of Washington. 2008.

Hudson K.S., K.L. Ulmer, P. Zimmaro, S.L. Kramer, J.P. Stewart, and S.J. Brandenberg. "Unsupervised Machine Learning for Detecting Soil Layer Boundaries from Cone Penetration Test Data." *Earthquake Engineering and Structural Dynamics*. Vol. 52, No. 11. pp. 3,201–3,215. DOI: 10.1002/ege.3961. 2023a.

Hudson, K.S., S.J. Brandenberg, P. Zimmaro, K.J. Ulmer, S.L. Kramer, and J.P. Stewart. "Relationship Between Fines Content and Soil Behavior Type Index at Liquefaction Sites." *Journal of Geotechnical and Geoenvironmental Engineering*, In press. DOI: 10.1061/JGGEFK/GTENG-12146. 2023b.

Idriss I.M. and R.W. Boulanger. "Examination of SPT-based Liquefaction Triggering Correlations. *Earthquake Spectra*. Vol. 28, No. 3, pp. 989–1,018, 2012.

Idriss, I.M. and R.W. Boulanger. "Soil Liquefaction During Earthquakes." D. Becker, ed. Earthquake Engineering Research Institute. 2008.

Marcuson III, W. F., and W.A. Bieganousky. "SPT and Relative Density in Coarse Sands. *Journal of the Geotechnical Engineering Division.* Vol. 103, No. 11. pp. 1,295–1309. 1977.

Moss, R.E., R.B. Seed, R.E. Kayen, J.P. Stewart, A. Der Kiureghian, and K.O. Cetin. "CPT-based Probabilistic and Deterministic Assessment of In Situ Seismic Soil Liquefaction Potential." *Journal of Geotechnical and Geoenvironmental Engineering*. Vol. 132, No. 8. pp.-1,032–1,051. 2006.

NGL. "Next Generation Liquefaction Database." 2021. <a href="https://www.nextgenerationliquefaction.org/">https://www.nextgenerationliquefaction.org/</a>>.

Phoon, K.-K. and F.H. Kulhawy. "Characterization of Geotechnical Variability." *Canada Geotechnical Journal.* Vol. 36, No. 4. pp. 612–624. NRC Research Press. https://doi.org/10.1139/t99-038. 1999.

Robertson, P.K. and K.L. Cabal. "Guide to CPT for Geotechnical Engineering." Signal Hill, California: 6<sup>th</sup> ed. Gregg Drilling Testing, Inc. 2015.

Saye, S.R., S.M. Olson, and K.W. Franke. "Common-origin Approach to Assess Level-ground Liquefaction Susceptibility and Triggering in CPT-compatible Soils using  $\Delta_Q$ ." *Journal of Geotechnical and Geoenvironmental Engineering.* Vol. 147, No. 7. 04021046. 2021.

Seed, H.B., K. Tokimatsu, L.F. Harder, and R.M. Chung. "Influence of SPT Procedures in Soil Liquefaction Resistance Evaluations. *Journal of Geotechnical Engineering.* Vol. 111, No. 12. pp. 1,425–1,445. 1985.

Seed, H.B. "Soil Liquefaction and Cyclic Mobility Evaluation for Level Ground During Earthquakes." *Journal of Geotechnical Engineering*. ASCE. Vol. 105, No, 2. pp. 201–255. 1979.

Skempton, A.W. "Standard Penetration Test Procedures and the Effects in Sands of Overburden Pressure, Relative Density, Particle Size, Ageing and Overconsolidation." *Geotechnique*. Vol. 36, No. 3, pp. 425–447. 1986.

- Stuedlein, A.W., B. Alemu, T.M. Evans, S.L. Kramer, J.P. Stewart, K. Ulmer, and K. Ziotopoulou. "PEER Workshop on Liquefaction Susceptibility." PEER Report 2023/02. Pacific Earthquake Engineering Research Center, UC Berkeley (headquarters). 207p. 2023.
- Ulmer, K.J., K.S. Hudson, S.J. Brandenberg, P. Zimmaro, R. Pretell, B. Carlton, S.L. Kramer, and J.P. Stewart. "Task 7C: Next Generation Liquefaction Models for Susceptibility, Triggering, and Manifestation." Washington, DC: U.S. Nuclear Regulatory Commission. March 2024.
- Wang, X., H. Wang, R.Y. Liang, and Y Liu. "A Semi-supervised Clustering-based Approach for Stratification Identification Using Borehole and Cone Penetration Test Data." *Engineering Geology*. Vol. 248. pp. 102–116. 2019.
- Wiecki, T., J. Salvatier, R. Vieira, M. Kochurov, A. Patil, M. Osthege, B.T. Willard, B. Engels, C. Carroll, O.A. Martin, A. Seyboldt, A. Rochford, L. Paz, R. Goldman, K. Meyer, P. Coyle, M.E. Gorelli, O. Abril-Pla, J. Lao, R. Kumar, V. Andreani, T. Yoshioka, G. Ho, T. Kluyver, K. Beauchamp, A. Andorra, D. Pananos, E. Spaak, B. Edwards, and E. Ma. "Pymc-devs/pymc: v5.9.1." 2023.
- Xie, J., C. Zeng, J. Huang, Y. Zhang, and J. Lu, J. "A Back Analysis Scheme for Refined Soil Stratification Based on Integrating Borehole and CPT Data." *Geoscience Frontiers.* Vol. 15, No. 1. 101688 pp. 2024.
- Youd, T.L., I.M. Idriss, R.D. Andrus, I. Arango, G. Castro, J.T. Christian, R. Dobry, W.D.L. Finn, L.F.J. Harder, M.E. Hynes, K. Ishihara, J.P. Koester, S.S.C. Liao, W.F.I. Marcuson, G.R. Martin, J.K. Mitchell, Y. Moriwaki, M.S. Power, P.K. Robertson, and K.H.I. Stokoe. "Liquefaction Resistance of Soils: Summary Report from the 1996 NCEER and 1998 NCEER/NSF Workshops on Evaluation of Liquefaction Resistance of Soils." *Journal of Geotechnical and Geoenvironmental Engineering*. Vol. 127, No. 10. pp. 817–833. doi: 10.1061/(ASCE)1090-0241(2001)127:10(817). 2001.

# **APPENDIX A**

Table A-1 Parameters in the Summary pkl File Containing SMT's Processed Case History Data

Parameter	Description	Classification
TEST_ID	primary key in test table	metadata
dGWT	depth to groundwater table (m)	layer
STRA_ID	Primary key in stratigraphy (STRA) table	metadata
STRA_TOP	depth to top of layer (m)	layer
STRA_BASE	depth to bottom of layer (m)	layer
STRA_USCS	USCS classification of the STRA layer	layer
STRA_COL	color description of layer	layer
STRA_DESC	text description of layer	layer
soil_type_all	soil type bin labels for all samples in the layer	layer
soil_type	representative soil type bin label for the layer	layer
Plhat_mu	mean of Box-Cox transformed PI hat	layer
Plhat_std	standard deviation of Box-Cox transformed PI hat	layer
Plhat_lambda	lambda for Box-Cox transformed PI hat	layer
PI	mean <i>PI</i> of the layer	layer
Plstd	standard deviation of <i>PI</i> in the layer	layer
Pls	measured PI values of specimens within the layer	layer
Plzs	depths of measured <i>PI</i> values within the layer (m)	layer
FC	mean FC of the layer	layer
FCs	measured FC values of specimens within the layer	layer
FCzs	depths of measured <i>FC</i> values within the layer	layer
sC	vertical total stress at the center of the layer (kPa)	layer
spC	vertical effective stress at the center of the layer (kPa)	layer

Table A-1 Parameters in the Summary pkl File Containing SMT's Processed Case History Data

Parameter	Description	Classification
zC	depth to the center of the layer (m)	layer
N	representative SPT blow count N of the layer	layer
Ns	measured SPT blow count <i>N</i> of samples in the layer	layer
Nzs	depths of the measured N values in the layer (m)	layer
CN	representative overburden normalization factor in the layer	layer
CNs	overburden normalization factors for individual <i>N</i> values in the layer	layer
CE	representative energy normalization factor in the layer	layer
CEs	energy normalization factors for individual <i>N</i> values in the layer	layer
N160cs	representative corrected <i>N</i> value (fines, overburden, energy correction) for the layer (l.e., average of "N160css" values)	layer
N160css	Individual corrected <i>N</i> values (fines, overburden, energy correction) within the layer	layer
PS	P[S] value associated with representative PI of the layer using the SMT's combined susceptibility model	layer
SITE_ID	primary key of site table	metadata
SITE_NAME	site name	metadata
TEST_NAME	test name	metadata
TEST_LAT	test latitude	metadata
TEST_LON	test longitude	metadata
EVNT_ID	primary key of event table	metadata
EVNT_NAME	event name	metadata

Table A-1 Parameters in the Summary pkl File Containing SMT's Processed Case History Data

Parameter	Description	Classification
EVNT_MAG	earthquake magnitude	profile
PGA	peak horizontal acceleration (g)	profile
FLDM_ID	primary key of fldm (field observation) table	metadata
FLDM_SFEV	surface evidence of liquefaction (0 = no, 1 = yes)	profile
FLDM_DIST	distance between observation and borehole (m)	profile
TEST Assignments	list of TEST_IDs grouped together with the same observation (FLDM_ID)	profile
TEST weights	weights for tests within a group of tests attached to the same FLDM_ID in the regression	profile
FLDM_SNBL	sand boils (0 = no, 1 = yes)	profile
CSR Lasley r_d	CSR computed using stress reduction coefficient from Lasley et al. (2017)	layer
MSF Green et al b=0.2	magnitude scaling factor from Green et al. (2019) for b = 0.2	layer
Ksig Carlton	$K_{\sigma}$ for SMT model	Layer`

#### **REFERENCES**

Green R.A., J.J. Bommer, A. Rodriguez-Marek, B.W. Maurer, P.J. Stafford, B. Edwards, P.P. Kruiver, P.P., G. De Lange, and J. Van Elk. "Addressing Limitations in Existing 'Simplified' Liquefaction Triggering Evaluation Procedures: Application to Induced Seismicity in the Groningen Gas Field." *Bulletin of Earthquake Engineering*. Vol. 17, pp.4,539–4,557. 2019.

Lasley, S. J., Green, R. A., & Rodriguez-Marek, A. "Number of Equivalent Stress Cycles for Liquefaction Evaluations in Active Tectonic and Stable Continental Regimes." *Journal of Geotechnical and Geoenvironmental Engineering.* Vol. 143, No. 4, 04016116. 2017.